IOP Concise Physics | A Morgan & Claypool Publication

Electromagnetics in Magnetic Resonance Imaging

Physical principles, related applications, and ongoing developments

Christopher M Collins

IOP | ebooks

Electromagnetics in Magnetic Resonance Imaging: Physical Principles, Related Applications, and Ongoing Developments

Electromagnetics in Magnetic Resonance Imaging: Physical Principles, Related Applications, and Ongoing Developments

Christopher M Collins
Department of Radiology,
New York University School of Medicine

Morgan & Claypool Publishers

ISBN 978-1-6817-4083-6 (ebook)
ISBN 978-1-6817-4019-5 (print)
ISBN 978-1-6817-4211-3 (mobi)

DOI 10.1088/978-1-6817-4083-6

Version: 20160301

IOP Concise Physics
ISSN 2053-2571 (online)
ISSN 2054-7307 (print)

A Morgan & Claypool publication as part of IOP Concise Physics
Published by Morgan & Claypool Publishers, 40 Oak Drive, San Rafael, CA, 94903, USA

IOP Publishing, Temple Circus, Temple Way, Bristol BS1 6HG, UK

To my parents, whose support and encouragement allowed me the flexibility and inspiration to flourish from before birth through my undergraduate years - and to my wife, whose companionship is both the incentive and reward for most everything I accomplish ever since.

Contents

Preface

As an undergraduate student studying engineering in the early 1990s, I became intrigued with electromagnetics. The idea of invisible, pervasive fields that could be described so well with a single set of equations coupled with the expectation that there must be beneficial applications to the human body was irresistible to me. At that time, magnetic resonance imaging (MRI) was not nearly the household term it is today, but without a doubt it was then and is now where electromagnetic fields meet the human body with ranges in strength and frequency found in no other single application.

I was fortunate to enter the field of MRI at a time when, first, numerical computations of electromagnetic fields were becoming feasible for geometries as complex as the human body at resolutions on the order of millimeters and, second, MRI in human subjects was entering a regime where electromagnetic wavelengths in human tissues would become smaller than the dimensions of the human body. I have greatly enjoyed using numerical methods to both explain the effects of field–tissue interactions as seen on MR images and evaluate potential health effects with greater accuracy than previously possible. Many of the figures in this work are the results of such simulations.

Through the years I have also greatly enjoyed seeing many people with backgrounds in engineering and electromagnetics enter the field of MRI and make their own mark on the field.

This book is but a transient attempt to concisely explain some of the most basic aspects of a very dynamic field. It is designed for a reader who has some familiarity with the principles of electromagnetics, but little or no understanding of how MRI is accomplished. Insights and explanations using basic sequences and applications are designed to be valuable to the reader towards understanding the present, and perhaps one day shaping the future of MRI.

Acknowledgements

Those to whom I am indebted for helping position me to write this book are certainly too numerous to count here. Nonetheless, I will try to name some of the most generous and influential in my life. Professor Vasundra Varadan, whose course in electromagnetics first sparked my love for the field(s); Professor Michael B Smith, whose interest in electromagnetics within MRI inspired him to invest in a fledgling student; Dr Steve Li and Professor Qing X Yang, for patience and insight in discussing the purpose and behavior of electromagnetic fields in MRI; Professor Kenneth R Foster for patience and insight in describing the mechanisms of interaction between electromagnetic fields and tissue and their importance wherever fields and tissues meet; Dr William A Edelstein for his quiet confidence that I, too, could make a significant impact in a field that had already changed medicine; Professor David I Hoult for patience and insight in mathematically demonstrating the need to consider field components counter to both precession and intuition; Professor Daniel K Sodickson, whose eternal enthusiasm for the infinite possibilities in MRI continues to drive imagination and progress in the field; and the numerous students and colleagues from throughout our scientific community with whom engaging questions and ensuing discussions have required improvement and refinement of both my own understanding and my ability to explain it.

Author biography

Christopher M Collins

Chris Collins was born in Park Ridge, Illinois. The son of a Navy nuclear engineer, he would live all across the US before beginning college. He received his Bachelor of Science degree in Engineering Science from The Pennsylvania State University (PSU), followed by his PhD in Bioengineering from the University of Pennsylvania in 1999. He continued his career at PSU's College of Medicine in Hershey, PA, until he joined the faculty at New York University's Center for Biomedical Imaging in Manhattan. Dr Collins' research has focused on the development of numerical approaches to simulate the electromagnetic fields in Magnetic Resonance Imaging (MRI) as they interact with the human body, and the resulting tissue heating and image artifacts, as well as in the application of these numerical methods to ensure safety and image quality in MRI.

IOP Concise Physics

Electromagnetics in Magnetic Resonance Imaging: Physical Principles, Related Applications, and Ongoing Developments

Christopher M Collins

Chapter 1

Fundamentals of MRI—fields and basic pulse sequences

In the past few decades, magnetic resonance imaging (MRI) has become an indispensable tool in medicine, with MRI systems now available at every major hospital in the developed world. But for all its utility and prevalence, it is much less commonly understood and less readily explained than other common medical imaging techniques. Unlike optical, ultrasonic, x-ray (including computed tomography (CT)), and nuclear medicine-based imaging, MRI does not rely primarily on simple transmission and/or reflection of energy, and the highest achievable resolution in MRI is orders of magnitude smaller that the smallest wavelength involved.

In this e-book, MRI will be explained with emphasis on the magnetic fields required, their generation, their concomitant electric fields, the various interactions of all these fields with the subject being imaged, and the implications of these interactions to image quality and patient safety. Classical electromagnetics will be used to describe aspects from the fundamental phenomenon of nuclear precession through signal detection and MRI safety. Simple explanations and Illustrations combined with pertinent equations are designed to help the reader rapidly gain a fundamental understanding and an appreciation of this technology as it is used today, as well as ongoing advances that will increase its value in the future. Numerous references are included to facilitate further study with an emphasis on areas most directly related to electromagnetics.

In this first chapter, the basic mechanisms exploited in MRI will be described with the use of fundamental equations of electromagnetics, moving quickly to a classical picture of a single hydrogen (^{1}H) nucleus (a single proton) as a spinning charged particle. From this starting point we will describe how applied magnetic fields interact with ensembles of nuclei, and what fields in what sequences can be applied to image the body.

doi:10.1088/978-1-6817-4083-6ch1

1.1 Proportionality of net nuclear magnetization to static magnetic field strength, $\mathbf{B_0}$

Before painting a classical picture of nuclear precession, it is first important to provide some fundamentals from the quantum mechanical description. Just as light can be described classically in terms of electromagnetic waves or quantum mechanically in terms of photons, so MRI has classical and quantum mechanical characteristics. Which description is preferred in a given circumstance often depends on the scale of interest and the phenomenon being described.

The hydrogen (^{1}H) nucleus, a single proton, has quantum mechanical properties including spin and charge. In the presence of an applied static magnetic field, $\mathbf{B}_0$, (having strength B_0) at any one time, each proton will be in either a high or low energy state, with a slight majority of the nuclei being in the low energy state. This lower energy state is where the magnetic moment of the nucleus (which, from the classical description to follow can be seen as a result of a spinning charge) is aligned with $\mathbf{B}_0$ ('spin-up') while the higher energy state is where its magnetic moment is aligned against $\mathbf{B}_0$ ('spin-down'). As B_0 increases, a larger fraction of the nuclei will be in the lower energy state, increasing the strength of the net nuclear magnetization vector at rest, $\mathbf{M}_0$. In fact, in the regime where MRI is performed on human subjects, the magnitude of $\mathbf{M}_0$ (M_0) is directly proportional to B_0. For pure water with temperatures and B_0 field strengths pertinent to MRI, $M_0 \approx 3.25 \times 10^{-3}$ A m^{-1} times B_0, where B_0 is expressed in tesla [1]. While it is possible, and sometimes necessary, to continue much further than this with quantum mechanical descriptions of the processes used in MRI, for the purposes of this book we will move directly to classical descriptions.

1.2 Classical description of nuclear precession

Although individual nuclei alternate between spin-up and spin-down states very rapidly, an ensemble of ^{1}H nuclei (or an ensemble of 'spins') in any appreciable volume collectively behave in a more stable manner that can be understood with the use of classical electromagnetics, remembering that in reality these classical descriptions require the actions of numerous nuclei acting separately. Here we will take advantage of the fact that in imaging of the human body there are always countless ($\sim 10^{19}$) hydrogen nuclei in any one cubic millimeter of tissue and begin with a simplified picture of a nucleus as a spinning sphere of charge. With this concept, it is possible to segment the sphere into numerous elemental spinning rings of charge, each of which acts as a loop of current.

Consider only a single elemental spinning ring of charge in the nucleus, represented by the loop in figure 1.1(a)–(c). In figure 1.1(a), $\mathbf{v}_n$, where n = 1–4, indicate velocities associated with the spinning motion at locations 1 through 4. We can first see that the Biot–Savart law dictates that, as a loop of current, this spinning ring of charge creates a small magnetic moment, $\mathbf{m}$ (figure 1.1(a)). As a review, the Biot–Savart law can be written

$$\mathrm{d}\mathbf{B} = \frac{\mu I \mathrm{d}\mathbf{L} \times \mathbf{a}_r}{4\pi r^2}$$

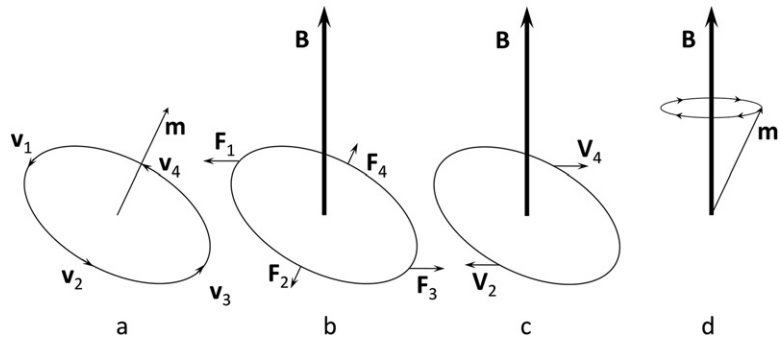

Figure 1.1. Graphical depiction of the physical origin of nuclear precession.

where d**B** indicates the contribution to the total magnetic field at one location by an electrical current of strength I as it travels through the short segment d**L**, and where the vector $\mathbf{a}_r$ indicates the direction from the location of d**L** to that where the magnetic field is being calculated, r indicates the distance between these two locations, and μ is the magnetic permeability of the medium. Thus, in figure 1.1(a), the vectors $\mathbf{v}_n$ can be thought of as different segments d**L**, for the electrical current created by the spinning ring of positive charge, and the contribution from each of them to the magnetic field at the center of the ring can be shown to point in the direction of **m** by using the right-hand rule. This is accomplished by pointing the thumb of the right hand in the direction of the first vector in the cross product (d**L** here, oriented with $\mathbf{v}_n$ in figure 1.1(a)) such that the long bones of the hand are oriented in the direction of the second vector of the cross product ($\mathbf{a}_r$ here, pointing from $\mathbf{v}_n$ to the center of the loop in figure 1.1(a)), at which point the fingers of the right hand, when oriented perpendicular to the long bones in the hand, indicate the direction of the vector on the other side of the equality from the cross product (d**B** here, in the same direction of **m** in figure 1.1(a)), for all $\mathbf{v}_n$ as well as any other location on the loop in between.

When the nucleus is placed in an applied magnetic field, **B** in figure 1.1(b), we can utilize the equation $\mathbf{F} = q\mathbf{v} \times \mathbf{B}$ (and, again, the right-hand rule) to examine the forces acting on the ring as a result of its spinning motion in the applied field (figure 1.1(b)). The forces at two of these locations, location 2 and location 4, are equal and opposite and along the same line, and thus have no net effect. The other two, at locations 1 and 3, are equal and opposite and along different lines, and can be seen to create a 'moment'.

While in figure 1.1(b) we have only shown force vectors at four specific locations, in reality a point charge traveling from location 4 to location 2 will experience a force having a component in the direction of $\mathbf{F}_1$ the entire time it travels over the upper half of the loop. The amplitude of that component will increase from zero at location 4 to a maximum at location 1 and then decrease to zero again when approaching location 2. Knowing that $\mathbf{F} = m\mathbf{a}$, (where m indicates the mass of the point charge and **a** is acceleration) we see that this point charge will be accelerated in the direction of $\mathbf{F}_1$ the entire time it travels over that top portion of the loop, reaching a maximum secondary 'precessional' velocity, $\mathbf{V}_2$ in that direction when it

reaches location 2. Similarly, a point charge traveling from location 2 to location 4 along the lower portion of the loop will experience acceleration in the direction of $\mathbf{F}_3$ the entire time it travels through that portion, reaching a maximum precessional velocity in the direction of $\mathbf{F}_3$ when it reaches location 4. The maximum precessional velocities from placing the spinning ring of charge into the magnetic field are shown in figure 1.1(c), with the resulting effect of precessional motion on the magnetic moment produced by the spinning ring of charge shown in figure 1.1(d).

Note that for a stronger applied magnetic field, the forces would be stronger, and so would the frequency of the precessional motion. The proportionality between precessional frequency and the strength of the applied magnetic field, B, can be described with the Larmour equation,

$$f_{\mathrm{L}} = \gamma B$$

where f_{L} is called the Larmour frequency and γ is the gyromagnetic ratio. For ^{1}H, the nucleus used exclusively for practically all clinical MRI examinations, $\gamma \approx 42.58$ MHz T^{-1}. Thus, precession of ^{1}H in a 1.5 T static magnetic (B_0) field would occur at approximately 64 MHz, and precession of ^{1}H in a 3 T B_0 field would occur at approximately 128 MHz.

Precession is perhaps more familiar as the 'wobble' of a toy top or a gyroscope in a gravitational field, the origins of which can be described in a similar manner to the description above for nuclei in a magnetic field, remembering that the effective force of gravity is translated to a moment about the location where the tip of the toy top or gyroscope rests on the ground. The proportionality between the precessional frequency and strength of the gravitational field, a parallel to the Larmour equation for nuclear precession, is also seen for the top or gyroscope. For example, a gyroscope on the moon will precess much more slowly than when on earth.

It is important to be comfortable with the basic concept of precession, because in MRI the desired primary effects of all the magnetic fields applied (static B_0 field, switched gradient fields, and radiofrequency (RF) B_1 field) on the resulting signal can be described in terms of either an additional precessional motion, or as an alteration in the frequency of the primary precession about $\mathbf{B}_0$.

It is also useful at this time to recognize that the effect of nuclear precession on $\mathbf{m}$ as described above and shown in figure 1.1(d) can be described with an equation of the form

$$\mathrm{d}\mathbf{m}/\mathrm{d}t = \mathbf{m} \times \mathbf{B}$$

where $\mathbf{B}$ can be any applied field in any direction.

1.3 Manipulating M in a static $\mathbf{B_0}$ field with an RF ($\mathbf{B_1}$) pulse

While in figure 1.1 we present the effect of a field on a single elemental ring of a charged, spinning nucleus, in matter (such as human tissue) there are countless nuclei in every cubic millimeter (about 6.7×10^{19} in pure water), and while a slight majority of these nuclei will be oriented roughly in the same direction as a B_0 field oriented in the z-direction, the ensemble will have no net magnetization in the

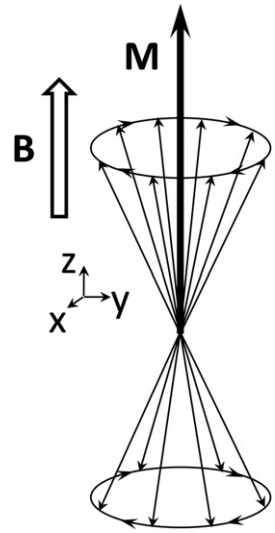

Figure 1.2. An ensemble of ^{1}H nuclei (the majority in the lower-energy, 'spin up' state) at one location precessing at equilibrium about a magnetic field **B** oriented in the longitudinal (z-oriented) direction will produce a static net magnetization **M** oriented in the longitudinal direction, but no net magnetization in the transverse (x–y) plane, and will thus produce no detectable RF signal.

transverse (laboratory x or y) directions, as illustrated in figure 1.2. We thus now return to **M**, the net magnetization vector. As mentioned in section 1.1, when at equilibrium in an applied static $\mathbf{B}_0$ magnetic field, $\mathbf{M} = \mathbf{M}_0$, is oriented with the applied $\mathbf{B}_0$ field (traditionally in the $+z$-direction), and (again) has strength $M_0 = 3.25 \times 10^{-3}$ A m^{-1} times B_0 in tesla [1]. Thus, no RF signal can be detected from the tissue at rest in a static magnet. In order to create an MR image we must first excite or perturb the system to a state where it produces a detectable signal. This can be accomplished by applying an RF magnetic ($\mathbf{B}_1$) field having a frequency equal to f_L and field components oriented perpendicular to $\mathbf{B}_0$.

Just as the components of any RF field in the transverse (x–y) plane can be separated into oscillating linearly polarized components B_{1x} and B_{1y} (oriented with x and y, respectively), they can also be expressed as circularly polarized components rotating clockwise and counter-clockwise within the transverse plane. The relationship between the rotating components, $B_{1\mathrm{ccw}}$ (appearing to rotate in a counter-clockwise direction when looking 'down' at it from a location in the $+z$-direction) and $B_{1\mathrm{cw}}$ (appearing to rotate in a clockwise direction when looking 'down' at it from a location in the $+z$-direction), and the linearly polarized components B_{1x} and B_{1y} can be expressed as [2]

$$\begin{aligned} B_{1\mathrm{ccw}} &= \left(B_{1x} + iB_{1y}\right)/2 \\ B_{1\mathrm{cw}} &= \left(B_{1x} - iB_{1y}\right)^*/2. \end{aligned} \tag{1.1}$$

The z-oriented component, B_{1z}, is the same whether using the rotating components ($B_{1\mathrm{ccw}}$, $B_{1\mathrm{cw}}$) or the oscillating components (B_{1x}, B_{1y}) in the transverse plane. Here all

components are complex quantities where, with phasor notation, both magnitude and phase are represented, and the asterisk indicates a complex conjugate.

One of the two rotating components will rotate in the same direction as nuclear precession, and will thus, assuming the frequency of the applied B_1 field matches f_L, appear as a static field in the frame of reference of the nuclei, rotating about z at a frequency f_L. This component is called B_1^+, and in the rotating frame of reference can be seen to induce a second precessional motion. Which of the two rotating components (B_{1ccw} or B_{1cw}) rotates in the same direction as nuclear precession and is thus equal to B_1^+ depends on the orientation of $\mathbf{B}_0$, which can in reality be in either the $+z$- or $-z$-direction for a given B_0 magnet. If B_0 is oriented in the $+z$-direction (as we assume here), nuclear precession will occur in a clockwise (or left-handed) sense about the $+z$-axis and thus B_1^+ will be equal to B_{1cw}. (It is important to be aware that in many works, B_1^+ is defined synonymously with B_{1ccw} and B_1^- is defined synonymously with B_{cw}, but due to the direction of nuclear precession about B_0, for B_1^+ to be defined by B_{1ccw}, B_0 would need to be oriented in the $-z$-direction, which is contrary to convention.)

To illustrate the second precession about B_1^+, we can draw the rotating frame as a Cartesian system with axes x', y', and z as shown in figure 1.3. Here the real portion of B_1^+ (having a phase of zero degrees from some reference phase) could be seen as the x'-component and the imaginary portion (having a phase that leads the reference phase by 90°) could be seen as the y'-component, such that the orientation of B_1^+ within the rotating frame would depend on the RF phase of the applied B_1 field. Assuming a B_1^+ field is applied with a phase such that it would lie on the x'-axis, the relationship $d\mathbf{M} = \mathbf{M} \times \mathbf{B}$ shows that this B_1 field would induce a precessional motion in the y'–z-plane of the rotating frame, as shown in figure 1.3.

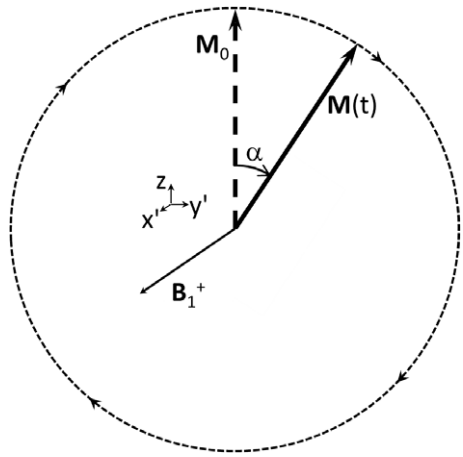

Figure 1.3. Precession of the net nuclear magnetic moment, **M**, about the circularly polarized component of an applied RF magnetic (B_1) field, $\mathbf{B}_1^+$, that is oriented with the x'-axis in a frame of reference rotating about the z-axis at the Larmour precession frequency. The flip angle is measured from the orientation of **M** at the start of the pulse, which is $\mathbf{M}_0$, oriented with the $\mathbf{B}_0$ field (in the $+z$-direction) at the beginning of the first pulse in an imaging sequence.

Remembering that $f_L = \gamma B$ and that for ^1H $\gamma = 42.58$ MHz T^{-1}, it is clear that the 'tip angle' α induced by a B_1^+ field in a 'rectangular pulse' having constant amplitude applied for a duration τ can be calculated as

$$\alpha = \gamma |B_1^+| \tau.$$

More generally, for a B_1 pulse that is 'on resonance' (having a frequency exactly equal to f_L),

$$\alpha = \gamma \int_{\tau}^{0} |B_1^+| \, dt \tag{1.2}$$

For example, with this equation it can easily be shown that to induce a 90° tip angle with a rectangular pulse having a duration of 3 ms, a B_1^+ field with a magnitude of about 2 microtesla (μT) will be required.

1.4 Free induction decay

While signal detection will be discussed again later in this book, even now it is possible to see that after the B_1^+ pulse just described is applied any amount of time resulting in a flip angle that is not some integer multiple of 180°, **M** will have a transverse component $\mathbf{M}_T$ that is perpendicular to the static B_0 field, and will rotate about $\mathbf{B}_0$ in the laboratory frame due to nuclear precession. Thus, $\mathbf{M}_T$ associated with a given small volume now appears something like a very small bar magnet rotating at the frequency $f_L = \gamma B_0$, and can produce a coherent, detectable RF signal in a nearby loop of wire, or receive coil, as illustrated in figure 1.4. This signal will decay with time as two 'relaxations' occur: (i) the spins return to their equilibrium state such that $\mathbf{M} = \mathbf{M}_0$, oriented with the applied $\mathbf{B}_0$ field ('spin-lattice relaxation', characterized with a time constant T_1) and (ii) the spins lose their coherent orientation with respect to each other in the transverse (x–y) plane. This second relaxation has different contributors, including 'spin–spin relaxation' and an additional 'dephasing' due to any spatial inhomogeneity in the applied $\mathbf{B}_z$ field (including $\mathbf{B}_0$ and gradient fields—to be discussed shortly).

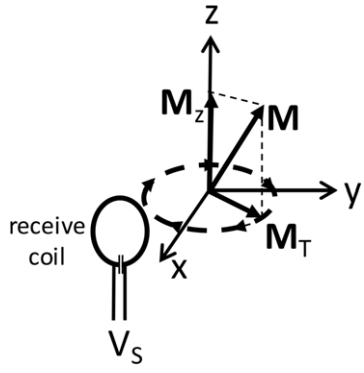

Figure 1.4. After excitation with an applied B_1 field, $\mathbf{M}_T$ (the transverse component of **M**) will precess about B_0, and can induce a detectable current in a nearby loop of wire or receive coil, resulting in a signal voltage, V_s.

Spin–spin relaxation can be understood by recognizing that the magnetic fields produced by individual nuclei will affect the total fields experienced by neighboring nuclei, causing them to precess at different frequencies from each other, and thus losing their coherence such that the component of **M** projected onto the transverse plane (M_T) will decay at a rate characterized by a time constant T_2. In pure liquid water, the random motion of nuclei relative to each other results in a situation where a single nucleus is almost as likely at any one time to be in a situation where the magnetic field from other nuclei increase the field it experiences (thus increasing its precessional frequency) as it is to be in a situation where neighboring nuclei decrease the field it experiences (decreasing its precessional frequency). Thus, over time, nuclei in pure liquid water stay in phase with each other a relatively long time (resulting in a long T_2) compared to, for example, nuclei in lipid, which are much more stationary with respect to each other, such that the effects of neighboring nuclei on each other are not likely to be reversed from one moment to the next and the signal becomes incoherent much faster.

For all materials important for human imaging, $T_1 > T_2$ so that the effects of these two relaxation processes on M in the presence of no applied fields but B_0 can be described mathematically with the equations

$$M_z(t) = M_0 - (M_0 - M_z(0))\mathrm{e}^{-t/T_1} \tag{1.3}$$

and

$$|M_T(t)| = |M_T(0)|\mathrm{e}^{-t/T_2} \tag{1.4}$$

where $M_T(0)$ indicates the amplitude of M_T immediately after the last applied B_1 excitation pulse or gradient pulse (having a possible range from 0 to M_0) and $M_z(0)$ indicates M_z immediately after the last B_1 pulse (having a possible range of $-M_0$ to M_0). Combining many of the concepts discussed so far we can now introduce the Bloch equation [3]

$$\frac{\mathrm{d}\mathbf{M}}{\mathrm{d}t} = \gamma(\mathbf{M} \times \mathbf{B}) - \left(\frac{M_x}{T_2}\mathbf{a}_i + \frac{M_y}{T_2}\mathbf{a}_j + \frac{M_z - M_0}{T_1}\mathbf{a}_k\right)$$

where γ is the gyromagnetic ratio, T_1 and T_2 are the longitudinal and transverse relaxation rates, respectively, M_0 is the magnitude of the net nuclear magnetization at rest aligned with and proportional to the strength of a given z-oriented static magnetic field ($\mathbf{B}_0$), and $\mathbf{a}_i$, $\mathbf{a}_j$, and $\mathbf{a}_k$ are unit vectors in the x-, y-, and z-directions. This equation is fundamental to MRI and will be referred to in subsequent sections. The left-most portion describes nuclear precession, or how we can manipulate M with applied fields, and the right-most three terms describe how M_{xy} relaxes to zero M_z relaxes towards its equilibrium state, equal to $\mathbf{M}_0$.

In the laboratory frame of reference with no fields applied but $\mathbf{B}_0$, M_T at each location will appear as a small magnet that rotates at f_L, and whose strength decays with time. By Faraday's law,

$$\oint_l \mathbf{E} \cdot \mathrm{d}\mathbf{l} = -\iint_s \frac{\partial}{\partial t}\mathbf{B} \cdot \mathrm{d}\mathbf{s}.$$

The magnetic field **B** associated with $\boldsymbol{M}_T$ can thus induce an RF electrical field in a nearby loop of wire resulting in an electrical current that will oscillate at f_L and decay with time. In the absence of any applied fields but $\mathbf{B}_0$, the resultant decaying signal is called 'free induction decay'.

Assuming that B_0 is perfectly homogeneous, the behavior of **M** can be described with the Bloch equation as shown above. In reality, however, B_0 is not perfectly homogeneous. In fact, just the minute differences in the magnetic susceptibilities of different biological materials throughout the body cause inhomogeneity in B_0 resulting in variations in f_L throughout the tissue. This causes the signal to become 'de-phased', resulting in the nuclei becoming incoherent and $\boldsymbol{M}_T$ losing magnitude at a faster rate than indicated by T_2 alone. If the variation in the B_0 field across one image voxel can be described as ΔB, this faster rate of signal decay is denoted by T_2^* where [4]

$$\frac{1}{T_2^*} = \frac{1}{T_2} + \frac{1}{\Delta B}.$$

1.5 Slice-selective excitation

Knowing that $f_L = \gamma B$ and that in order to excite **M** to a point where it produces signal the frequency of an applied B_1 pulse must match f_L, we can excite only a portion of a large three-dimensional (3D) sample, such as the human body, by in effect making B_0 a function of position so that only nuclei precessing in the range of frequencies contained in the B_1 pulse will become excited.

A single 'slice' of tissue with a desired thickness can be excited, then, by making B_z a function of position such that f_L increases linearly with position while applying a B_1 pulse with a range of frequencies matching those of f_L in the desired slice. Making B_z a function of position is accomplished with the use of magnetic field gradients, G_x, G_y, and G_z, (often expressed in millitesla per meter, or mT m^{-1}) which can be controlled independently in three orthogonal directions such that

$$B_z(x, y, z, t) = B_0 + xG_x(t) + yG_y(t) + zG_z(t).$$

Note that the gradient magnetic fields added to B_0 at each location through time ($xG_x(t)$, $yG_y(t)$, and $zG_z(t)$) ideally have only a z-oriented component which varies in strength linearly with position. The field gradients G_x, G_y, and G_z are typically designed such that the origin ($x = y = z = 0$) is at the center of the imaging volume and that moving in one direction from the origin will give fields that add to B_0 and moving in the other direction will produce fields that oppose it. Also note that with addition of G_x, G_y, and G_z of different amplitudes, it is possible to create a linear field gradient in any desired direction.

For a first example describing a basic method for accomplishing imaging, we will assume that we want to map the signal from a single slice of tissue in a transverse or 'axial' plane—meaning a plane perpendicular to the axis of the B_0 magnet, which is most often cylindrical in shape with the z-axis along its center. To accomplish this we can apply a z-oriented gradient such that $B_z = B_0 + zG_z(t)$. For this example, let us suppose that B_0 is 1.5 T and G_z is 50 mT m^{-1}, and we wish to excite a slice that is

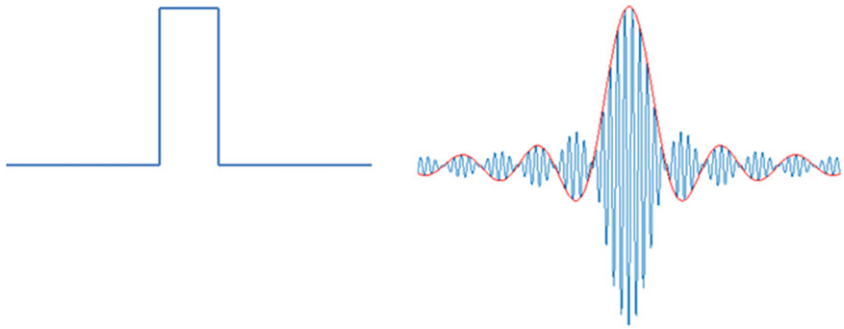

Figure 1.5. Desired frequency profile of a rectangular slice excitation profile (left) and the center portion of the sinc-modulated B_1 pulse shape in time needed to produce it (right). Here the B_1 pulse is shown with the RF coil currents in blue. The coil currents, as well as B_x and B_y oscillate at f_L. The amplitude of B_1^+, however, will vary with the red line, or the envelope of the RF pulse.

5 mm thick centered about $z = 0$. With $f_L = \gamma B$, we can show that in that slice, ^{1}H nuclei will precess at frequencies from about 63.8647 MHz to about 63.8753 MHz when the gradient is applied. To excite **M** in this slice only, we need to apply a B_1 pulse with a frequency centered at 63.87 MHz and having a bandwidth of about 10.6 kHz.

While there are a number of considerations in practical pulse design, for this example, let us assume we wish to excite M within this slice (and corresponding frequency range) the same amount while not exciting M outside of this slice at all. The result is a rectangular profile in the frequency domain, as shown on the left side of figure 1.5. To define the B_1 pulse in the time domain that could produce this rectangular 'slice excitation profile', we must perform an inverse Fourier transform of it. Doing so produces a B_1 pulse with a center frequency at f_L and a sinc-shaped modulation in the time domain, as shown on the right side of figure 1.5.

While the sinc function ($\text{sinc}(x) = \sin(x)/x$) is defined infinitely in each direction, in practice it is necessary to truncate it. RF pulses are often designed as (for example) sinc3 or sinc5 where the number (3 or 5) indicates the number of zero crossings on each side of the center before truncation. The result of truncation in the time domain is a frequency excitation profile having a less-than-ideal rectangular profile.

While there are many RF pulse shapes used in MRI, it is worth mentioning here the sinc pulse, Gaussian pulse, and rectangular pulse. Gaussian and sinc pulses are often used in the presence of an applied field gradient for slice-selective excitation. If it is desired to excite an entire volume, a very brief, strong, rectangular pulse (often called a 'hard' pulse) can be used with no gradients applied. Figure 1.6 shows some common RF pulse shapes and their corresponding slice excitation profiles.

Figure 1.7 shows a simple pulse diagram for a slice-selective pulse with its associated gradient pulse. Note that a negative gradient pulse is applied for a brief duration following the RF pulse. This is required to 're-phase' the spins. During the RF pulse the slice-selection gradient, G_z in this example, was applied to accomplish slice selection as described above, by making the frequency of nuclear precession a function of location. Because spins at different locations in the direction of the gradient are precessing at different rates during the application of this pulse, however,

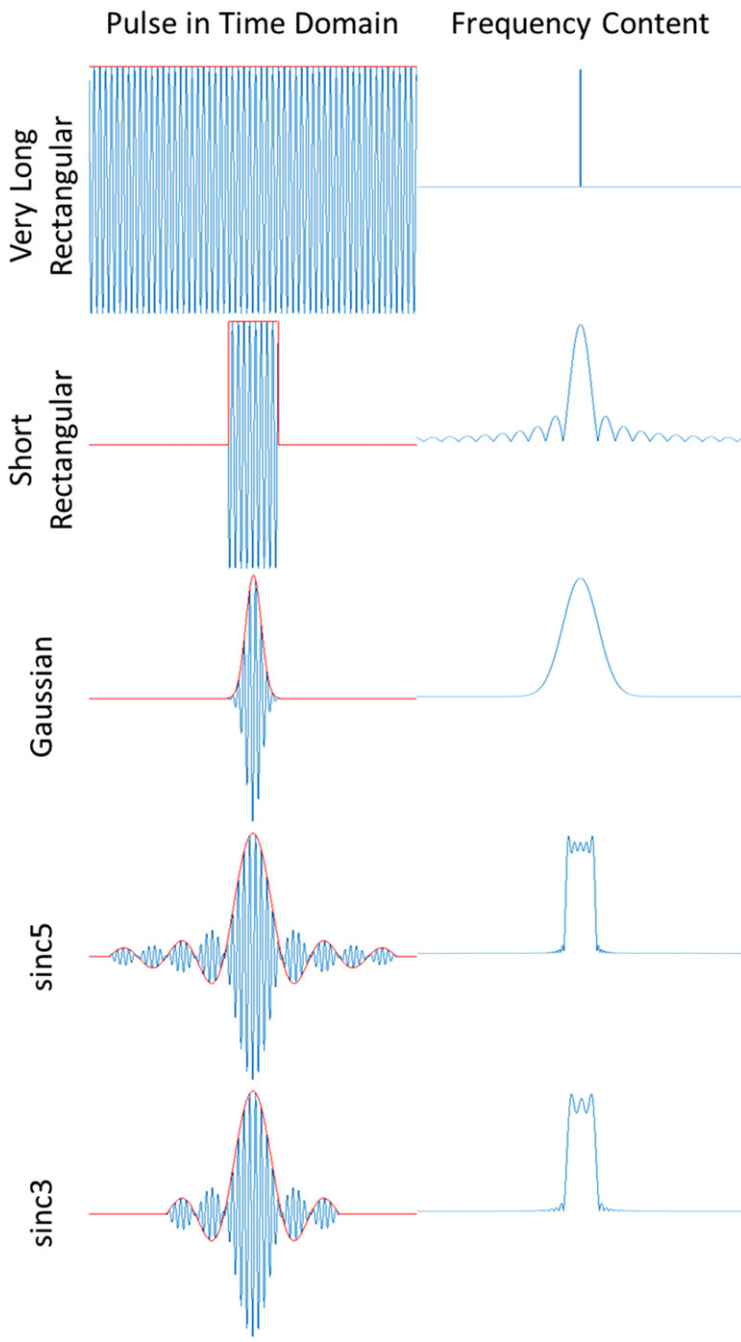

Figure 1.6. Different excitation pulses (left) and their slice excitation profiles (right).

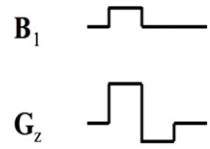

Figure 1.7. Slice selective pulse including negative refocusing lobe in gradient pulse.

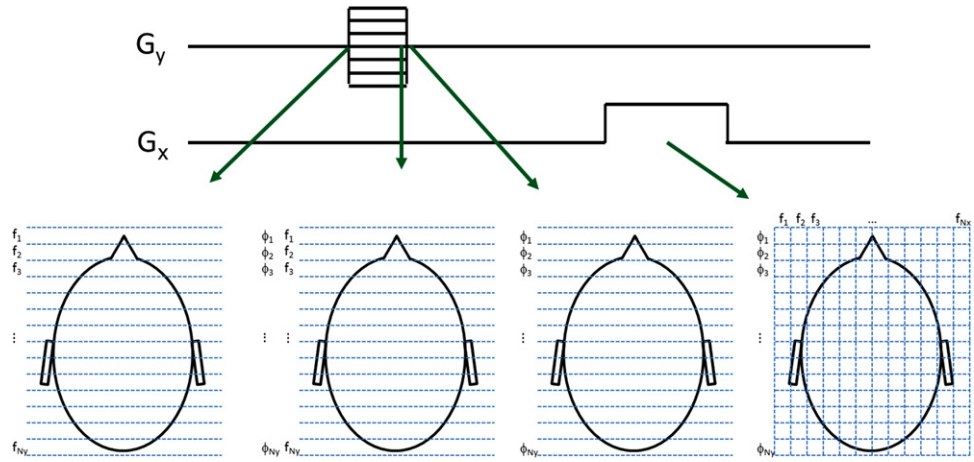

Figure 1.8. Illustration of frequency and phase encoding. In this example, during each repetition, N_x complex data points are acquired as a function of time during a single repetition.

they become de-phased from one another during this gradient pulse. Applying a negative gradient pulse with approximately one half the area of the primary pulse will effectively re-phase the spins after excitation for maximum signal strength.

1.6 Encoding spatial information into the net magnetization

In the preceding section we discussed how to excite all **M** within a particular slice of tissue with defined thickness, location, and orientation with an example where a 5 mm thick slice centered about $z = 0$ was excited. In order to map the signal from **M** at locations within this slice and thus create a two-dimensional (2D) image, we must encode spatial information onto **M** throughout the slice. In the most basic forms of MRI (what we will call 'fundamental acquisition'), two different encoding methods are often used: frequency encoding and phase encoding. Stated very simply, for frequency encoding, a field gradient is applied during signal acquisition so that f_L in the detected signal is a function of location in one direction, and for phase encoding a field gradient is applied for a finite duration of time before signal acquisition so that the phase of the signal is a function of position in another direction (conventionally a direction orthogonal to that used for frequency encoding).

Figure 1.8 illustrates the effects of frequency- and phase-encoding gradients applied in orthogonal directions on a single slice of tissue. When the phase-encoding gradient (G_y in this example) is first turned on, the precessional frequency will vary

linearly with position in the y-direction, indicated with frequencies f_1 to f_{Ny}. By the end of the phase-encoding gradient pulse there will have been phase evolution proportional to the precessional frequency (or location in y) and the duration of the pulse, indicated with ϕ_1 to ϕ_{Ny}. When the frequency-encoding gradient (G_y in this example) is then turned on and data is acquired, frequency will be a function of position in the x-direction, indicated with f_1 to f_{Nx}. Since only N_x data points are acquired in a single repetition, the process must be repeated N_y times with unique strengths of G_y to acquire enough data for an N_x by N_y image. In figure 1.8, the lines above the illustration showing the timecourse of the RF and gradient pulses represent a simple pulse sequence diagram.

Remember that if M has different phases at different locations, it is incoherent and produces a lower signal than if M had the same phase at all locations. Phase encoding, which is designed to make the phase of M a function of location, by nature causes a reduction in the strength of the acquired signal. In order to maximize the signal during frequency encoding and signal acquisition, however, it is possible to 'pre-wind' the phases with a negative gradient pulse in the frequency-encoding direction before applying the frequency-encoding gradient and acquiring the signal. This results in a signal 'echo', where there is a maximum in the signal near the middle of the acquisition period. Figure 1.9 illustrates the formation of a gradient echo. To cause a gradient echo near the middle of the acquisition period, the negative pre-winding pulse in the frequency-encoding gradient should have one half the area (amplitude integrated over time) as the area during frequency encoding and

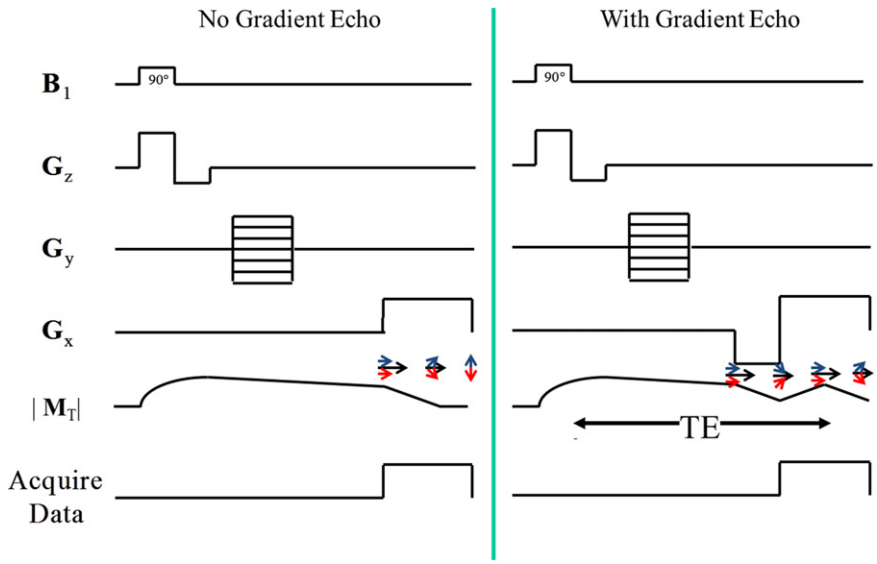

Figure 1.9. Formation of a gradient echo. The blue and red arrows indicate $\mathbf{M}_T$ in the rotating frame of reference at different locations in the frequency-encoding (x) direction, such that they precess at different frequencies during application of the frequency-encoding gradient, leading to dephasing and a reduction in M_T (represented by the black arrow). Application of a negative pre-winding gradient pulse in the frequency-encoding direction results in re-phasing of spins during acquisition, for detection of significantly more signal.

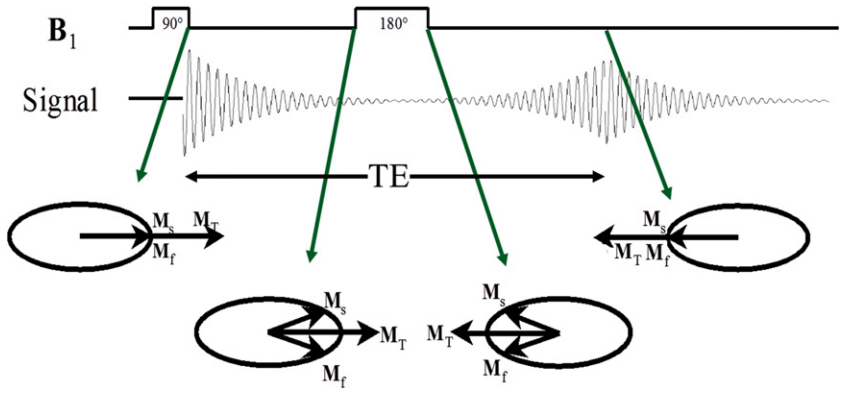

Figure 1.10. Formation of an spin echo with application of a 180° refocusing pulse.

signal acquisition. Note that the time between the RF excitation pulse and the echo is called 'echo time' and has the abbreviation TE. Due to the decay of signal, in general a shorter TE will allow for stronger signal to be acquired, but greater contrast between tissues resulting from tissue-dependent T_2 (or T_2* for a gradient-echo sequence) can result from longer TE.

With a 180° 'refocusing pulse' applied after RF excitation and before signal acquisition, it is possible to also reverse the signal-reducing effects of B_0 inhomogeneities, resulting in a 'spin echo' [5]. Figure 1.10 illustrates the formation of a spin echo. Here M_f and M_s indicate the transverse components of magnetization vectors from nuclei precessing faster and slower than they would in a field at exactly B_0 due to inhomogeneities in the B_0 field. Applying a 180° pulse half-way between the time of RF excitation and the mid-point of signal detection results in M_f being re-located 'behind' M_s such that it will 'catch up' to M_s and the signal will be rephrased during signal acquisition.

Note that in an spin echo pulse sequence, the pre-winding pulse in the frequency-encoding gradient to produce a gradient echo is also present, but to save time in the sequence and allow for a short TE, this pulse can appear before the refocusing (180°) B_1 pulse. Because the refocusing pulse effectively reverses all the phases of M_T, the pre-winding pulse will not appear negative with respect to the frequency-encoding gradient if it is positioned before the refocusing B_1 pulse.

Assuming that only a single RF coil is used for detection, during a single signal acquisition period in a scheme such as that discussed so far, typically a number of complex data points (containing information of amplitude and phase) equal to the number of desired image pixels in the frequency-encoding direction, N_x, is acquired. In order to form a 2D image with fundamental acquisition, however, it is necessary to acquire a number of unique data points equal to the total number of pixels in the final image, or N_x times the number of desired image pixels in the phase-encoding direction, N_y. In fundamental acquisition this is accomplished by repeating the sequence of pulses and the acquisition a number of times equal to N_y with a different (unique) strength of G_ϕ in each repetition. The time between repetitions is called TR. The resulting pulse diagram for a spin echo sequence might look something like figure 1.11.

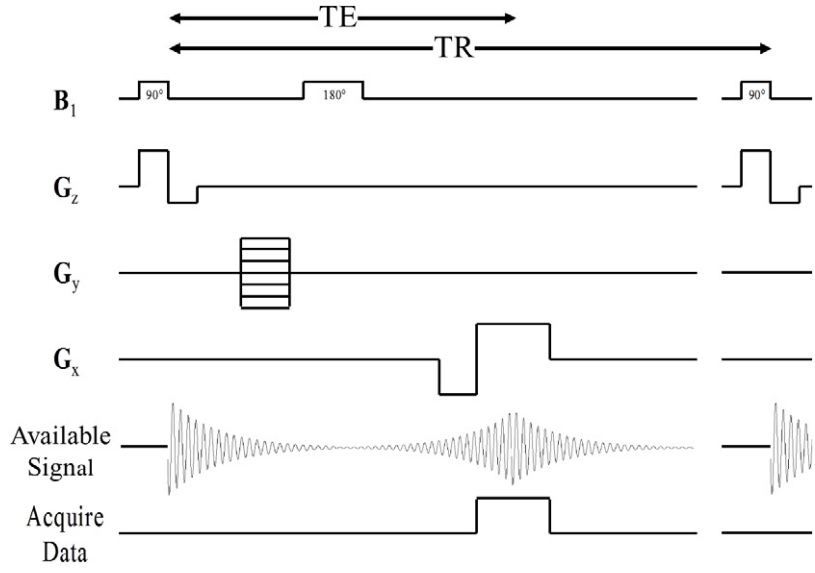

Figure 1.11. Pulse diagram for a spin echo sequence.

Note that in pulse sequence diagrams the change in amplitude of the phase-encoding pulse is typically indicated with having pulses with all their different amplitudes drawn in the same space, although only one strength is used in any given repetition.

Conceptually, we have now discussed all the basic ingredients required for image acquisition. There are, however, some other practical issues for acquiring images that are worthy of at least brief mention at this time. First, if TR is not long enough that all available signal (M_T) has decayed before the next repetition, it can be necessary to eliminate this residual M_T before the next repetition so that it does not confound the process of spatial encoding. One way to accomplish this is with the application of very strong gradients to completely de-phase M_T. Next, in cases where TR is not long enough that M_z will recover to its initial state ($\mathbf{M} = \mathbf{M}_0$) by the end of each repetition, the excitation tip angle producing maximal signal for the image may be notably smaller than 90°.

1.7 Introduction to *k*-space for simple image acquisition and reconstruction

As described in the previous sections, the signal as induced in an RF coil during MRI is oscillatory with a frequency near f_L, with spatial information encoded into the frequency and phase of this signal through space and time. Typically preamplifiers very near the coil ensure the signal-to-noise ratio (SNR) is great enough that additional noise and signal degradation from cables during transfer of the signal have negligible effect on SNR before the signal reaches the 'spectrometer', where a variety of signal processing steps occur. First, a central frequency very close to an average f_L for the entire sample when no gradients are applied is subtracted from the RF signal with use

of a frequency mixer. After this, the frequency and phase of the signal are ideally only a function of the applied gradients and any inhomogeneities in B_0, but not of B_0 itself. An analog-to-digital converter then digitizes the signal, allowing for the use of digital filters to remove noise from outside the desired receive bandwidth.

After these basic signal conditioning steps are taken, the signal is arranged into a multidimensional array of complex data (containing magnitude and phase information), referred to as '*k*-space'. Location in *k*-space is described with orthogonal dimensions, k_x, k_y, and k_z, containing information about spatial frequency (for example, having units of cm^{-1}) in the *x*-, *y*-, and *z*-directions in image space (for example, having units of cm). In the examples discussed so far, where only a single transverse slice is imaged, *k*-space is 2D in k_x and k_y only.

To understand the mathematical relationship between *k*-space and image space, consider the signal received in a single coil during an imaging sequence such as those discussed till now, where signal acquisition occurs after phase encoding in the *y*-direction and during frequency encoding in the *x*-direction. At each point in time during signal acquisition, the signal at any acquisition time point comes from the entire excited slice, and can be described with the spatial-encoding equation [6]

$$S\left(G_y,\, \tau_{\text{pe}},\, G_x,\, t\right) = \int_{y_{\min}}^{y_{\max}} \int_{x_{\min}}^{x_{\max}} \rho(x,\, y) \mathrm{e}^{-j\gamma G_y y \tau_{\text{pe}}}\, \mathrm{e}^{-j\gamma G_x x t}\, \mathrm{d}x\mathrm{d}y$$

where ρ (often called simply 'proton density') contains location-specific, time-dependent available signal intensity as a function of the tissue properties and sequence parameters (including T_1, T_2, TE, TR, flip angle, etc), and the signal at each location and time is affected by the previously applied spatial phase-encoding gradient (having strength G_y and duration τ_{pe}) and the ongoing spatial frequency-encoding gradient (having strength G_x and having begun time t before the present time).

Now, defining

$$k_x = \frac{\gamma}{2\pi} G_x t$$

and

$$k_y = \frac{\gamma}{2\pi} G_y \tau_{\text{pe}},$$

we can rewrite the encoding equation

$$S\left(k_x, k_y\right) = \int_{y_{\min}}^{y_{\max}} \int_{x_{\min}}^{x_{\max}} \rho(x,\, y) \mathrm{e}^{-j2\pi k_x x}\, \mathrm{e}^{-j2\pi k_y y}\, \mathrm{d}x\mathrm{d}y$$

which is easily recognizable as a Fourier transform from space (x and y having dimensions of cm) to spatial frequency (k_x and k_y having dimensions of cm^{-1}).

There are a number of fundamental, useful relationships between *k*-space and image space. In fundamental acquisition, the number of data points required in a given direction in *k*-space (N_{kx}, N_{ky}, N_{kz}) is equal to the number of data points in the

corresponding desired image (the number of pixels or voxels) with the number of image pixels or voxels in the corresponding dimension in image space (N_x, N_y, N_z)

$$N_{kx} = N_x$$
$$N_{ky} = N_y$$
$$N_{kz} = N_z.$$

The desired image resolution in a given spatial dimension (Δx, Δy) is equal to the inverse of the range of spatial frequencies present in the corresponding dimension in k-space

$$\Delta x = \frac{1}{\max(k_x) - \min(k_x)}$$
$$\Delta y = \frac{1}{\max(k_y) - \min(k_y)}$$
$$\Delta z = \frac{1}{\max(k_z) - \min(k_z)}$$

and there is a similar inverse relationship between the desired field of view (FOV) in the image in each direction ($x_{\max} - x_{\min}$, $y_{\max} - y_{\min}$, $z_{\max} - z_{\min}$) and the resolution of spatial frequency in k-space (Δk_x, Δk_y, Δk_z)

$$\Delta k_x = \frac{1}{x_{\max} - x_{\min}}$$
$$\Delta k_y = \frac{1}{y_{\max} - y_{\min}}$$
$$\Delta k_z = \frac{1}{z_{\max} - z_{\min}}.$$

These relationships, coupled with the understanding that the current location in k-space is determined by the history of applied gradients in each repetition, allow for both a good understanding of how to design a pulse sequence to achieve an image of desired FOV and resolution, as well as allowing for great creativity in how to acquire the data necessary for such an image.

For example, in the acquisition described previously, a 2D array in k-space could be populated with data by filling one line in the direction corresponding to frequency encoding with the data acquired during each repetition and with a new line in k-space shifted in the direction corresponding to phase encoding acquired during each repetition with a new phase-encoding gradient strength. Again, the number of data points acquired during each repetition would be equal to the number of desired pixels in the frequency-encoding direction N_x, and the number of repetitions with different phase-encoding gradient strengths would be equal to the number of desired pixels in the phase-encoding direction. The way that all of k-space would be filled during the sequence could be illustrated as in figure 1.12.

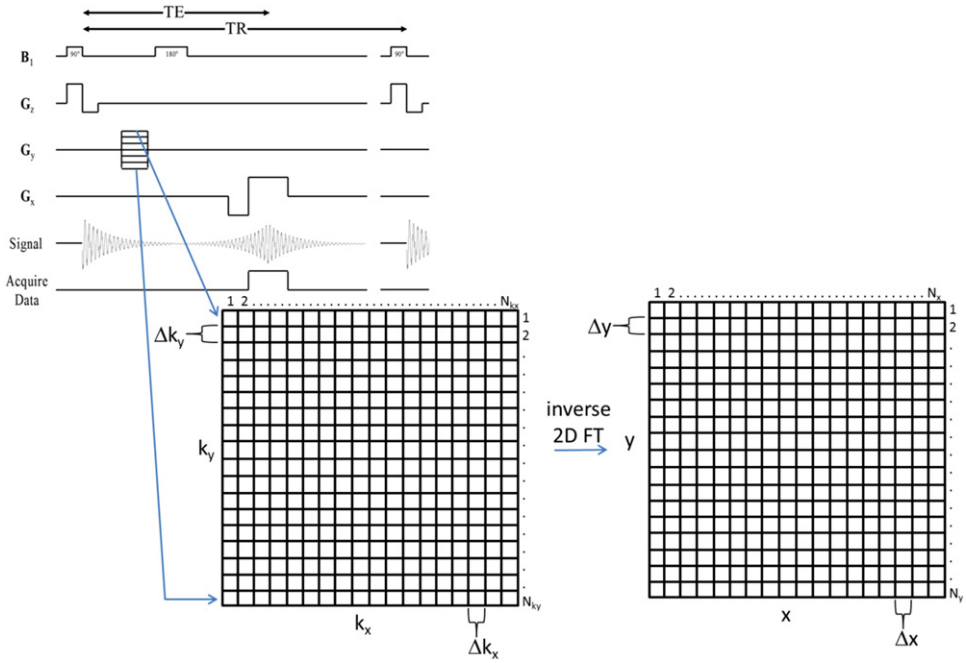

Figure 1.12. Filling 2D *k*-space with data from a 2D image acquisition.

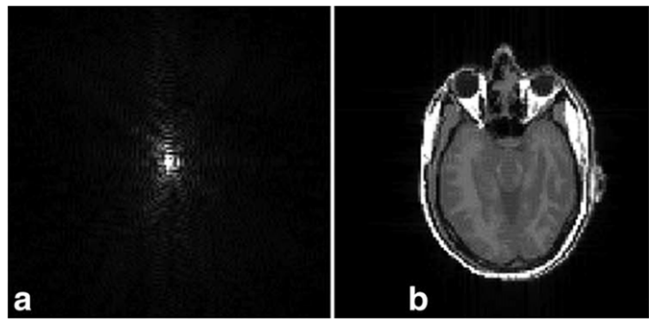

Figure 1.13. Amplitude of data in *k*-space (a) and, after a 2D inverse Fourier transform of the complex data, the resulting magnitude image (b).

Properly acquired and arranged, this data in *k*-space approximates a 2D Fourier transform of the desired image. By nature, it will have large amplitudes near the middle, containing low-spatial-frequency information (as with minimal or no gradient dephasing), and smaller amplitudes near the edges, containing high-spatial-frequency information (as when strong gradients have been applied for some time). Thus, the desired image, with amplitude and phase as functions of position in space, is reconstructed by applying a 2D inverse Fourier transform to the 2D array in *k*-space, as shown in figure 1.13.

Note that the acquired signal is complex, having amplitude and phase, and thus also is its representation in k-space before the inverse Fourier transform and in image space after the transform. For the majority of clinical imaging, the image displayed is the amplitude of the data in the image domain, but (as will be discussed), for some cases and in some situations the phase information is also very valuable.

There are some practical considerations for this type of image acquisition that should be mentioned here. During the repetitions with maximum positive and negative strength of the phase-encoding gradient (often the first and last repetitions in an image acquisition of this type), in order to avoid aliasing (or mis-mapping of signal due to redundancy in phase labelling, e.g., 0° and 360°), the edges of the FOV in the phase-encoding direction should encompass the entire object being imaged and the strength of the applied phase-encoding gradient should be defined such that the phase encoding of M_T will range from π to $-\pi$ across the image space in the phase-encoding direction, resulting in the relationship

$$\mathrm{FOV}_y = \frac{1}{\Delta k_y} = \frac{2\pi}{\gamma \Delta G_y t_{\mathrm{pe}}}.$$

Related to aliasing, the phase-encoding direction is necessarily defined such that the edges of the image in that direction will be outside the boundaries of the object being imaged. While for frequency encoding, signal from regions of tissue outside the desired image can be removed with a bandpass filter, this is not the case for phase encoding. Also, in a situation such as imaging the chest on a transverse plane, where the sample does not cross any edges of the desired FOV and the sample is shorter in one direction than the other, the direction chosen for phase encoding is often that of the shorter dimension of the sample, allowing for fewer phase-encoding steps (and thus fewer repetitions and a shorter imaging time) required to acquire all necessary data with the desired spatial resolution.

The concept of k-space is especially useful in designing pulse sequences to acquire all the necessary data with a wide range of schemes. Location in k-space at a given time depends on the strength and duration of gradients applied until that time. For example, figure 1.14 shows the portion of the pulse sequence pertaining to G_x and G_y in the first repetition of the above spin echo sequence along with a map of the trajectory in k-space where different colors are used to indicate what portion of the path taken in k-space indicates what gradient is applied. Here dotted lines indicate travel in k-space without acquiring data and solid lines indicate travel occurring while filling k-space with data.

Now consider a case where we would like to fill several lines of k-space in a single repetition. This can be accomplished with an echo planar imaging (EPI) sequence [7] like that illustrated in figure 1.15 along with its k-space trajectory map.

Finally, consider a spiral trajectory [8], as shown in figure 1.16. Even though this sequence does not use a traditional concept of different phase- and frequency-encoding directions, once k-space is filled the image can be produced with a 2D Fourier transform (after some interpolation to translate to Cartesian coordinates).

From this progression it should be possible to imagine how a wide variety of sequences might be designed to acquire the necessary data to construct images. This might include a radial acquisition, using only frequency-encoding gradients resulting

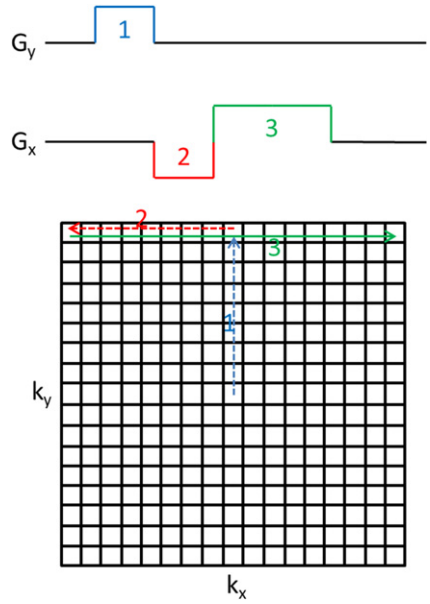

Figure 1.14. Trajectory in *k*-space (bottom) resulting from in-plane encoding gradients applied in a single TR of the sequence of figure 1.12 (top). Dotted (blue and red) lines indicate travel without acquisition, solid (green) lines indicate acquisition (during frequency encoding in this case).

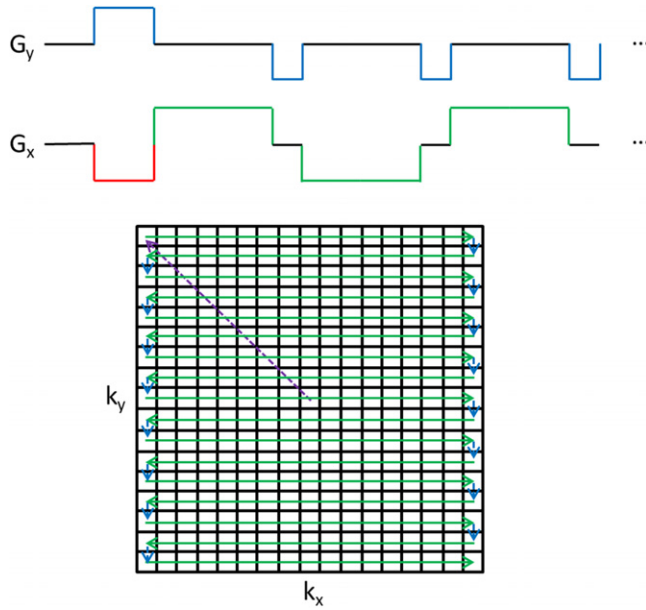

Figure 1.15. In-plane encoding gradient pulses for an EPI sequence (top) and resulting trajectory in *k*-space (bottom). Dotted (purple and blue) lines indicate travel without acquisition, solid (green) lines indicate acquisition (during frequency encoding in this case).

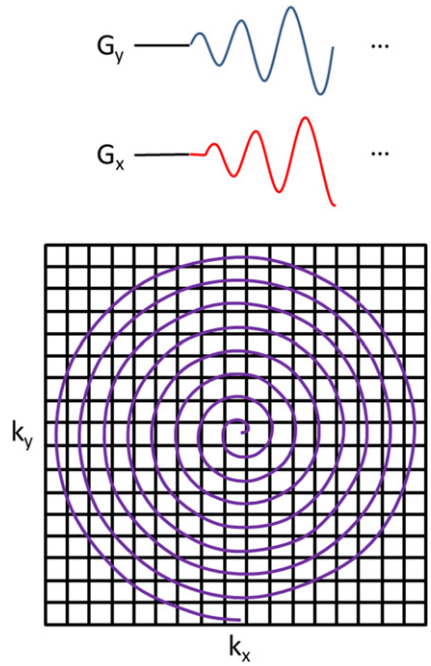

Figure 1.16. In-plane gradient encoding pulses for a spiral imaging sequence (top) and resulting trajectory in *k*-space (bottom). Data are acquired during the entire trajectory.

in a series of acquisitions oriented in a wide range of angles in *k*-space, or even 3D trajectories covering entire volumes.

1.8 Imaging slices with arbitrary orientations and 3D volumes

Until now, the process of MRI has been described with a desired 2D imaging plane being 'transverse' or 'axial' (parallel to the *x*–*y* plane). This included a *z*-oriented gradient field to excite an axial slice, but it would also be possible to use an *x*-directed gradient to excite a 'sagittal' slice, a *y*-directed gradient to excite a 'coronal' slice, or any combination of the three to excite an 'oblique' slice having any other orientation. Similarly, combinations of the gradient fields could be used to accomplish phase and frequency encoding in directions orthogonal to that of the slice-selection gradient.

Figure 1.17 illustrates the conventional orientation of the human body with respect to Cartesian coordinates in a typical MRI system. The *x*-axis is parallel to the left–right direction in the human body, the *y*-axis is parallel to the front–back (or 'anterior–posterior') direction in the human body, and the *z*-axis is oriented parallel to the head–foot (or 'inferior–superior') direction in the human body. Here a 'transverse' or 'axial' slice would be parallel to the *x*–*y* plane, a 'sagittal' slice would be parallel to the *y*–*z* plane, and a 'coronal' slice would be parallel to the *x*–*z* plane.

Different methods can be used to acquire images covering 3D volumes. The first, and most common, is a multi-slice acquisition, where each 'slice' produces a single 2D image. Here the excitation, encoding, and acquisition of signal for one slice

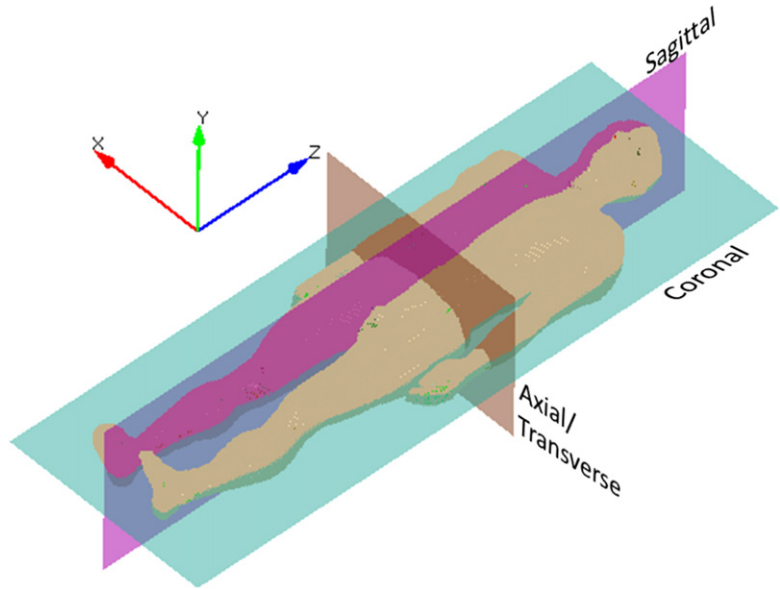

Figure 1.17. Conventional orientation of Cartesian coordinates with respect to the human body in MRI.

occur during the recovery period for the other slices. With this interleaved acquisition scheme, a number of slices roughly equal to TE/TR can be acquired in about the same time required for a single image.

The second approach to imaging entire volumes is 3D imaging, and requires defining a strategy to fill 3D *k*-space after excitation of a 'slab' (like a very thick slice) of tissue. Generally, 3D acquisitions are less common than multi-slice acquisitions in clinical imaging due to both the longer time required and the resulting greater likelihood for patient motion (including respiration and pulsatile blood flow) to adversely affect the image. 3D imaging has the potential advantage of a greater SNR because there are a greater number of acquisitions of signal from each location in the tissue.

1.9 Basic image contrast: proton density, T_1, and T_2 weighted spin echo images

Unlike other medical imaging methods, MRI is sensitive to a large number of different physical phenomena. The main tissue-specific physical characteristics discussed so far are T_1 relaxation rate, T_2 relaxation rate, and M_0. The first two quantities are expressed in milliseconds as the decay rates expressed in (1.3) and (1.4), while the last quantity is often referred to as simply 'proton density', and can be expressed as a fraction of the value for water. Table 1.1 gives the proton density, T_1, and T_2 for select tissues at both 1.5 T and 3 T.

By varying TE and TR in a spin echo sequence, it is possible to adjust the sensitivity of the signal intensity to these three basic characteristics in the final image.

Table 1.1. T_1, T_2, and proton density of select tissues at 1.5 T and 3 T [9–13]. Proton density is expressed as a fraction of that for pure water, T_1 and T_2 values are in milliseconds.

		1.5 T		3 T	
Tissue	Proton density	T_1	T_2	T_1	T_2
Cartilage	0.94	1024	42	1168	37
Skeletal muscle	0.95	1084	37	1416	41
Blood	0.97	1441	308	1932	275
Fat	0.94	343	160	382	130
Cerebrospinal fluid	1.0	4550	60	4550	30
Brain white matter	0.99	688	81	833	68
Brain grey matter	1.0	1195	97	1436	93

Table 1.2. Relative TE and TR in a spin echo image for different basic types of image contrast.

	TE	TR
Proton density weighted	Short	Long
T_1 weighted	Short	Short
T_2 weighted	Long	Long

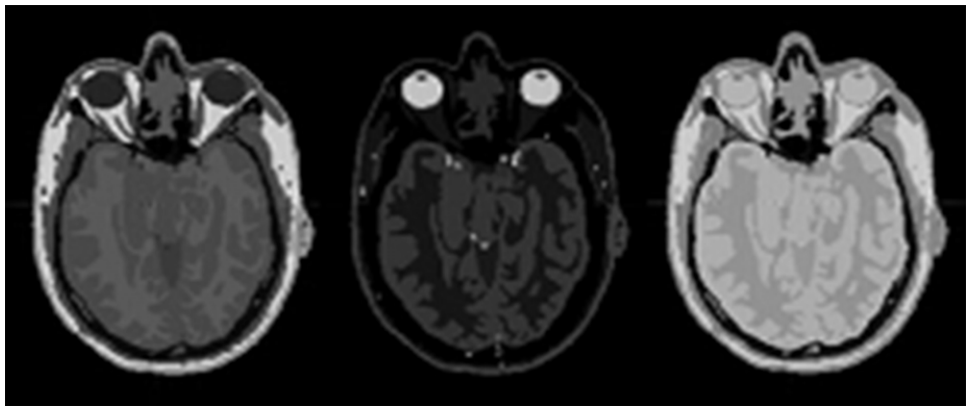

Figure 1.18. T_1 weighted (left), T_2 weighted (center), and proton density weighted (right) images.

If TR is long enough that the net nuclear magnetization approaches its equilibrium state in all tissues and at the same time TE is short enough that effects of different T_2 are not allowed to evolve, the signal is weighted strongly by proton density. Proton density weighted images have inherently high signal in all tissues, but relatively low contrast between them.

If TR is short enough that only tissues with short T_1 can recover significant M_z via T_1 relaxation in a single TR, and TE is short enough that effects of different T_2 are not allowed to evolve, the signal is strongly weighted by T_1 relaxation, resulting in a T_1 weighted image. Tissues such as fat with a short T_1 appear bright in this type of image.

If TR is long enough that the net nuclear magnetization approaches its equilibrium state in all tissues and at the same time TE is long enough that the different T_2 decay rates in tissue are allowed to evolve, the result is a T_2 weighted image. Tissues such as blood and cerebrospinal fluid having a long T_2 appear bright in this type of image.

Table 1.2 lists the relative TE and TR for accomplishing these three different image contrasts, while figure 1.18 shows simulated images containing them.

References

[1] Hoult D I and Lauterbur P C 1979 The sensitivity of the zeugmatographic experiment involving human samples *J. Magn. Reson.* **34** 425–33

[2] Hoult D I 2000 The principle of reciprocity in signal strength calculations—a mathematical guide *Concepts Magn. Reson.* **12** 173–87

[3] Bloch F 1946 Nuclear induction *Phys. Rev.* **70** 460

[4] Ordidge R J, Gorell J M, Deniau J C, Knight R A and Helpern J A 1994 Assessment of relative brain iron concentrations using T_2-weighted and T_2^*-weighted MRI at 3 tesla *Magn. Reson. Med.* **32** 335–41

[5] Hahn E L 1950 Spin echoes *Phys. Rev.* **80** 580

[6] Ben-Eliezer N, Shrot Y and Frydman L 2010 High-definition, single-scan 2D MRI in inhomogeneous fields using spatial encoding methods *Magn. Reson. Imaging* **28** 77–86

[7] Stehling M K, Turner R and Mansfield P 1991 Echo-planar imaging: magnetic resonance imaging in a fraction of a second *Science* **254** 43–50

[8] Glover G H 1999 Simple analytic spiral *k*-space algorithm *Magn. Reson. Med.* **42** 412–5

[9] Wright P J *et al* 2008 Water proton T_1 measurements in brain tissue at 7, 3, and 1.5 T using IR-EPI, IR-TSE, and MPRAGE: results and optimization *Magn. Res. Mater. Phys. Biol. Med.* **21** 121–30

[10] de Bazelaire C M, Duhamel G D, Rofsky N M and Alsop D C 2004 MR imaging relaxation times of abdominal and pelvic tissues measured *in vivo* at 3.0 T: preliminary results 1 *Radiology* **230** 652–9

[11] Diakova G, Korb J P and Bryant R G 2012 The magnetic field dependence of water T_1 in tissues *Magn. Reson. Med.* **68** 272–7

[12] Duck F A 2013 *Physical Properties of Tissues: A Comprehensive Reference Book* (New York: Academic)

[13] Cao Z, Park J, Cho Z H and Collins C M 2015 Numerical evaluation of image homogeneity, signal-to-noise ratio, and specific absorption rate for human brain imaging at 1.5, 3, 7, 10.5, and 14 T in an 8-channel transmit/receive array *J. Magn. Reson. Imaging* **41** 1432–9

IOP Concise Physics

Electromagnetics in Magnetic Resonance Imaging: Physical Principles, Related Applications, and Ongoing Developments

Christopher M Collins

Chapter 2

Fundamentals of Signal-to-Noise Ratio (SNR)

The SNR at each location in an image depends greatly on the strength of the magnetic fields applied through time at the corresponding location in the human body, the sensitivity of the receive coil(s) to transverse net nuclear magnetization there, and the electric fields throughout the body. Here we describe these relationships with intuitive rationale for conventional MRI.

2.1 Signal strength as a function of static and RF magnetic fields

As mentioned in section 1.4, the rotation of M_T in the laboratory frame of reference can induce electrical currents in a nearby conductor, thus inducing a detectable electrical signal. In MRI, signal detectors are, in fact, typically conductive wires, strips, or tubes shaped and positioned to be receptive to this signal, and interspersed with capacitors to resonate at f_L and maximize the induced current. These detectors are called 'RF coils'. For example, some of the first volumetric RF coils were long inductors constructed by coiling single conductors into a solenoidal shape. In MRI of humans today, RF coils with more specialized structures and arrangements have all but replaced the solenoid. Further discussion of RF coils is given in a later section of this book, but here we devote some time to use of the principle of reciprocity to determine the sensitivity distribution of a single MRI coil to M_T throughout space.

As mentioned in section 1.3, just as a transverse RF field can be separated into x- and y-oriented components, it can be separated into two counter-rotating circularly polarized components. It is clear that the circularly polarized component $\boldsymbol{B}_1$ that rotates in the same direction as nuclear precession is the component that will interact with the nucleus to induce a desired flip angle, and this component we call B_1^+.

What is not as readily obvious is that if we were to drive a receive coil, it would be the resulting field component rotating *opposite* nuclear precession that indicates the coil's sensitivity to signal induced by M_T throughout space. We call this counter-rotating component B_1^-.

doi:10.1088/978-1-6817-4083-6ch2

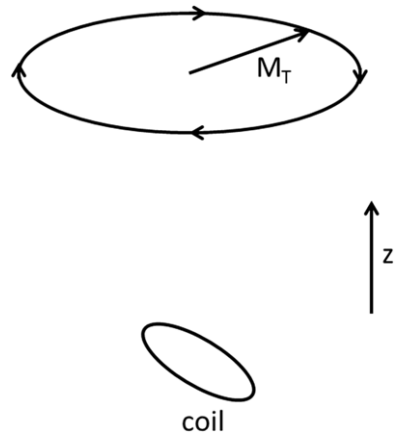

Figure 2.1. Intuitive Illustration pertaining to the need for counter-rotating circularly polarized field components in transmission and reception. The circularly polarized component of a wave traveling from the coil to interact with M_T in the sample must be left-handed in nature (with thumb pointing in the direction of propagation and fingers curved in the direction of polarization matching the rotation of M_T), while a circularly polarized wave produced by M_T and traveling to the coil would be right-handed in nature.

Early observations that it is the counter-rotating component B_1^- that indicates a coil's receptivity distribution [1] were not universally accepted [2]. It was not until much more recently, as B_0 reached 7 T, that this phenomenon became prominent enough that, after renewed discussion [3–5], it became well accepted [6]. While various mathematical explanations have been given [3, 5], here the simple illustration of figure 2.1 will suffice.

As mentioned in section 1.1, the amplitude of M is proportional to that of B_0. Via Faraday's law, the strength of the current induced in an RF coil will be proportional to f_L, which is also proportional to B_0. Assuming all other things remain constant, these two different mechanisms combined allow us to expect an increase in signal strength proportional to the square of B_0, and allow us to express the calculated signal voltage as [7]

$$V_{\text{signal}} = 2\pi f_L \int M_T B_1^- \mathrm{d}V.$$

This equation is very valuable, but has some limitations. For a gradient echo sequence with a very short TE and very long TR such that little T_2 relaxation occurs during each TE and nearly complete T_1 relaxation occurs during each TR (as in a proton density weighted image), M_T is proportional to the sine of the flip angle induced by B_1^+ during the excitation pulse. For simplicity, assuming a rectangular pulse shape with duration τ, in this situation, $M_T \approx M_0 \sin(\gamma B_1^+ \tau)$.

For other sequences, T_1, T_2, T_2^*, chemical content (e.g., fat versus water), sequence parameters including TE and TR, and voxel size also affect M_T. Furthermore, T_1, tissue electrical properties, and B_1 field distributions for a given coil are all functions of B_0, making it such that this relationship is not simple with

respect to field strength. Of course, it is not purely signal strength, but the ratio of signal to noise that determines the quality of an image.

2.2 Noise and intrinsic SNR

In MRI, noise comes from random thermal motion of particles from the molecular to the subatomic level which can result in random voltages at the terminals of the receive coil(s). Typically we only need to consider two sources of such thermal noise: random motion of charges in the conductive RF coils used for signal reception (coil noise) and random motion of ions and dipoles in the subject being imaged (sample noise).

Noise in MRI can be relatively easily related to Johnson noise as described by Nyquist [8]. In short, the greater the effective resistance of the coil, the greater the coil noise. Recognizing that for a given coil current, the effective resistance is proportional to the power dissipated, we can write

$$V_{\text{noise}} = \sqrt{4k\Delta\nu\left(T_{\text{sample}}P_{\text{sample}} + T_{\text{coil}}P_{\text{coil}}\right)}$$

where k is the Boltzman constant, $\Delta\nu$ is the receive bandwidth (a sequence-specific parameter equal to the bandwidth of all received signal from the sample, approximately equal to the strength of the frequency-encoding gradient times the FOV in the corresponding direction times γ), and where P_{sample} and P_{coil} are the amount of power dissipated in the coil and sample, respectively, when the coil is driven with one Ampere of current. Here the power dissipated in the receive coil and sample can be estimated at the frequency of interest for resonant coils by looking at the quality factors of the coil when empty and when loaded by the sample, or calculated from electrical fields, for example

$$P_{\text{sample}} = \int_V \sigma E^* \cdot E \mathrm{d}v,$$

so that, to a first approximation (for the sake of a somewhat intuitive explanation),

$$V_{\text{noise}} \propto \int_V \sqrt{\sigma}\|E\|\mathrm{d}v.$$

It is important to recognize that the receive coil is not actually driven during reception and we use the concept of dissipated power to relate to noise based on the principle of reciprocity. An intuitive understanding of the value of these equations using resistance (or power) and the mechanism by which noise is induced in the coil can be gained by considering that, by the principle of reciprocity, the electric field distribution associated with a given coil, E, will be proportional to the coil's sensitivity to small electrical currents due to moving ions and rotating dipoles throughout the sample, or to moving charges in the coil. If we consider the sample conductivity to be proportional to the number of ions, charges, or dipoles moving in the coil or sample at any one time per unit volume, then the likelihood that at any one time a certain number of charges will have moved in a given direction relative to the others becomes akin to a probability problem, and as with flipping N identical coins, the total tally of one outcome versus another is expected to typically remain

within the square root of the number of coins. That is, the amplitude of the noise voltage will increase with the square root of the conductivity [9]. With this in mind, for 1 A of current in the coil, the noise resistance for the sample is proportional to an integral of the square root of the sample conductivity (proportional to amplitude of random fluctuations) times the amplitude of the electric field of the coil (proportional to sensitivity to noise), bringing us to the square root of dissipated power.

A useful concept used often in MRI is that of intrinsic SNR, or ISNR [10], where many of the details of image-acquisition-specific effects on the signal (TE, TR, T_1, T_2, T_2^*) are removed or ignored, leaving primarily the fundamental effects of B_0, B_1^+, B_1^-, and noise. The resulting trends with B_0 can be thought of as the trends we would expect to see in a hypothetical image acquisition with very long TR and very short TE such that M always returns to M_0 before the excitation in the next repetition, and the signal does not have time to decay with T_2 or T_2^* before data are acquired in any repetition.

Although, as indicated in the previous section, we might expect the signal strength of a given number of spins with a given flip angle to increase with the square of B_0, the behavior of ISNR as a function of B_0 depends also on the behavior of noise as a function of frequency (which is different for coil noise and sample noise), as well as whether we are in a quasi-static regime where the B_1 field distributions are essentially independent of B_0 field strength (and thus B_1 frequency), or if we are in a high field regime, where the dependence of B_1 field distribution on B_0 field strength is more significant.

An often quoted expectation is for SNR to increase linearly with B_0. This expectation comes from the behavior of ISNR in a quasi-static regime where sample noise is dominant. The quasi-static regime in MRI is where electromagnetic wavelengths associated with f_L are very long compared to the dimensions of the human body, or where the magnetic field distribution for a certain coil carrying a given current is practically independent of f_L. In this regime, the distributions of both B_1^+ and B_1^- are independent of frequency so we can write

$$\mathrm{ISNR} \propto \frac{B_0^2}{\sqrt{P_{\mathrm{sample}}}}.$$

Assuming electric fields are induced by the RF B_1 field, we can use Faraday's law to recognize that in the quasi-static regime, $E \propto f_L$, or $E \propto B_0$, such that $P_{\mathrm{sample}} \propto B_0^2$. This then allows us to write simply

$$\mathrm{ISNR} \propto \frac{B_0^2}{\sqrt{B_0^2}} \propto B_0.$$

It should be noted that this often-quoted relationship also neglects to account for the fact that electrical conductivities of tissues generally increase with frequency, which would lead to a greater than quadratic relationship between P_{sample} and B_0 and a less-than-linear increase in ISNR with B_0.

Of course, outside of the quasi-static regime where sample noise is dominant, ISNR cannot be simplified so easily. The upper limit of this regime for imaging of

humans is at about 3 T, where wavelength effects become apparent in the head and body (where wavelengths are much shorter than in free space). The lower limit of this regime is somewhere below 0.5 T, where coil noise begins to be significant in comparison to sample noise [7]. Coil noise also becomes more significant as coils become very small compared to the sample. A more general expression (again, relevant to gradient echo sequence with short TE and long TR) would be

$$\mathrm{ISNR} \propto \frac{B_0^2 \sin\left(\gamma B_1^+ \tau\right) B_1^-}{\sqrt{P_{\mathrm{sample}} + P_{\mathrm{coil}}}}$$

where B_1^-, P_{sample}, and P_{coil} are all defined for the same driving condition of the receive coil. Both analytically and numerically based methods have been used to evaluate trends in ISNR with B_0 for a wide range of circumstances [11–15].

2.3 Quantitative calculation of SNR from electromagnetic fields

With careful consideration it is also possible to calculate a quantitative SNR for a given coil, sample, and pulse sequence. While this can be achieved with very sophisticated methods utilizing the Bloch equation for specific pulse sequences for realistic field distributions throughout anatomical models [16, 17], here we will perform an analytically based evaluation for the sake of being able to give a very explicit example.

Consider a situation where, with a 1 T MRI system, we desire to image a spherical sample having dimensions and electrical properties similar to the average in the human brain (15 cm diameter, ε_r of 116, and σ of 0.4 S m^{-1} at $f_{\mathrm{L}} = 42.58$ MHz). Assume that we will image this sample with a solenoidal coil of 30 cm diameter having about nine turns such that when it carries 1 A of current it produces a nearly homogeneous linear B_1 field having a strength of about 12 μT. Assuming a perfectly homogeneous B_1 field distribution we can calculate the magnetically-induced electric field induced throughout the sample when the coil carries 1 A using Faraday's law in integral, time harmonic form

$$\oint_l \mathbf{E} \cdot \mathrm{d}\mathbf{l} = -j\omega \iint_s \mathbf{B} \cdot \mathrm{d}\mathbf{s}.$$

Using this equation and recognizing that here, with all magnetically-induced electric fields having only a circumferential component,

$$P_{\mathrm{diss}} = \iiint \frac{\sigma |E|^2}{2} \mathrm{d}V$$

it is possible to show that [7]

$$P_{\mathrm{sample}} = \frac{\pi (D/2)^5 \sigma \omega^2 B_1^2}{15}.$$

Thus, in our case, P_{sample} will be about 2.05 W when the RF coil carries 1 A.

Assuming the axis of the solenoidal RF coil, and thus the B_1 field, is oriented with the x-axis, we can easily calculate both B_{1cw} and B_{1ccw} (and thus both B_1^- and B_1^+) to be 6 μT when the RF coil carries 1 A (1.1). For simplicity, assuming a 1 ms rectangular excitation pulse with 6 μT B_1^+, we can expect a flip angle very near 90° (1.2). For a very long TR and a very short TE, we can assume M_T will be very close to M_0. Assuming M_0 of pure water (3.25×10^{-3} A m^{-1} times B_0), and we can calculate the SNR as the signal from one voxel divided by the noise from the entire sample.

$$\mathrm{SNR} = \frac{2\pi f_L M_T B_1^- \mathrm{d}V}{\sqrt{4k\Delta\nu T_{sample} P_{sample}}}.$$

If we are trying to image the sphere at a resolution of 2 mm in each direction (ignoring coil noise for this size sample), dV is 2 mm^3, or 8×10^{-9} m^3. Supposing we have a 50 kHz receiver bandwidth and a T_{sample} equal to that of normal core body temperature (310.15 K), we find the SNR for a single acquisition to be very close to 1—not suitable for a medically relevant image. For an image acquired with many repetitions, however, it will be higher since signal is acquired multiple times (with different phase-encoding gradients, for example), and the noise will be different in each, leading to an SNR proportional to the square root of the number of acquisitions. For example, if we were to image the entire plane using a standard spin echo sequence with a FOV of 25.6 cm in each direction, corresponding to 128 phase-encoding repetitions for our 2 mm voxel size, this would bring our SNR to 11.3. For medical purposes, however, we would prefer an SNR still higher. Acquiring a 3D image with 128 phase-encoding acquisitions in each direction would bring our SNR to 128. As mentioned earlier, however, such an acquisition would take a very long time compared to a multi-slice acquisition. Other simple approaches to increase the SNR include increasing the voxel size (resulting in a decrease in image resolution), use of a weaker read-out gradient to decrease the receiver bandwidth (which can result in stronger image artifacts, including the chemical shift artifact) or averaging multiple complete acquisitions (also lengthening the time required). In fact, medical images often have a larger through-plane dimension than in-plane resolution to achieve acceptable SNR. The benefit of imaging at higher field strength (section 2.2) is clearly apparent in this example, and use of receive arrays (to be discussed in section 2.5) would also be beneficial.

Note that there are some impractical aspects of this example. First, a solenoid of this size operating at 42.58 MHz is not practical, and imaging of the human body with a solenoidal RF coil in general is not feasible, as the axis of the solenoid must be perpendicular to the axis of the B_0 magnet to produce B_1 perpendicular to B_0. Also, solenoidal coils are different than many other types of coils used in MRI, in that they can have a significant additional 'conservative' electric field (arising from the electric potential on the wires) that is perpendicular to the magnetically induced electric field considered here [18]. Nonetheless, this example illustrates the process by which SNR can be calculated quantitatively for known field distributions. In practice these field distributions are calculated for realistic coils containing realistic representations of the human body using numerical methods [4, 13, 16–18].

2.4 Effects of image sequence parameters on SNR

Design and optimization of MRI sequences for specific purposes is full of trade-offs. As seen in the example of section 2.3, obtaining an adequate SNR can require compromises in image resolution and/or time. As discussed previously, a proton density weighted sequence results in strong signal from throughout the body, but in relatively little contrast between tissues. As such, it tends to have comparatively little value in clinical diagnosis. In fact, imaging sequences used clinically sometimes employ methods to suppress signal from some tissues altogether. One way to do this is with a 180° 'inversion' pulse before the excitation pulse, which orients M in the negative z direction. The time between the inversion pulse and the excitation pulse can then be selected to ensure M is exactly zero for one tissue. This is done most commonly to suppress signal from fat (STIR sequence) or from fluid (FLAIR sequence). In short, sequence optimization for desired contrast with adequate SNR and image resolution requires consideration of multiple competing factors.

2.5 Array reception

To maximize the SNR, it is beneficial to use receive coils that have a high receive sensitivity, which can be characterized by

$$\frac{B_1^-}{\sqrt{P_{\text{sample}}+P_{\text{coil}}}}.$$

Receive sensitivity is generally higher at the center of smaller coils, which are sensitive to noise from a smaller portion of the sample, but such a coil will also typically only have adequate B_1^- over a small region of the sample. Thus, multiple coils spaced strategically around the sample are used to obtain a high SNR over a large region. If the coils are too small, however, they will not have adequate sensitivity at depth in the sample. Thus, the ideal number and size of coils for imaging a particular portion of the anatomy depends on (among other things) both the morphology of that region of the anatomy and the B_0 (and thus f_L) of interest. Related to this, it is generally preferable to have coils large enough and close enough to the sample that $P_{\text{sample}} > P_{\text{coil}}$, such that each coil is 'sample noise dominant'. Thus, a lower limit to coil size in conventional MRI can be where P_{coil} becomes an appreciable fraction of P_{sample}.

In fundamental acquisition, signal acquired simultaneously with multiple RF coils can be combined in a variety of ways to accomplish different things, such as maximizing the SNR at each location in the final image, producing an image with a uniform SNR, or producing a homogeneous final image where the final signal intensity is not dependent on the RF field distribution of the receive coil [19].

One of the most practical, simple, and widely utilized reconstruction methods for RF coil arrays is the sum-of-squares method [19]. With this method, the complex signal for each of the N coils S_n (with $n = 1$ to N) for each location r in the reconstructed images is combined to create a new signal strength S_{sos} as

$$S_{\text{sos}} = \sqrt{\sum_{n=1}^{N} S_n^* S_n},$$

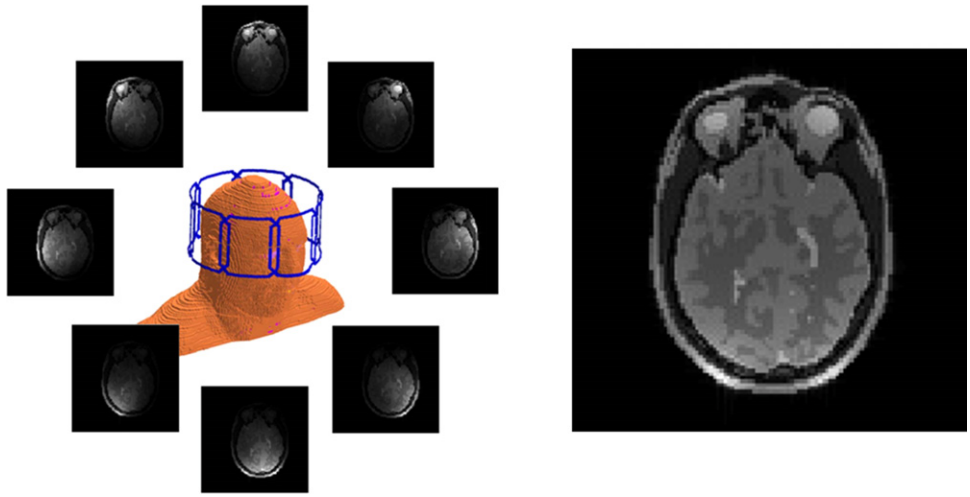

Figure 2.2. Array of receive coils (blue) surrounding head (orange) with individual images from each coil (left), and sum-of-squares image (right).

where the superscript asterisk indicates the complex conjugate. Figure 2.2 shows simulated images before and after applying a sum-of-squares reconstruction.

Although noise is distributed uniformly throughout an image acquired with a single coil, correlation of noise in the coils of an array (e.g. from the same random event in the sample inducing currents in more than one coil) can result in a more complex distribution of noise in images reconstructed with arrays [19], although it is evenly distributed across the image with the sum-of-squares method described above.

Today a very wide range of much more sophisticated array reconstruction methods are used that can remove signal weighting by the receive coil sensitivity distributions and even utilize receive coil sensitivity profiles to perform some spatial acquisition and thus reduce image encoding and acquisition time. In this book, these methods would be considered 'advanced' rather than 'fundamental' acquisition methods. Some of them are discussed very briefly in section 6.1.

References

[1] Glover G H *et al* 1985 Comparison of linear and circular polarization for magnetic resonance imaging *J. Magn. Reson.* **64** 255–70

[2] Tofts P S 1994 Standing waves in uniform water phantoms *J. Magn. Reson. B* **104** 143–7

[3] Hoult D I 2000 The principle of reciprocity in signal strength calculations—a mathematical guide *Concepts Magn. Reson.* **12** 173–87

[4] Collins C M, Liu W, Schreiber W, Yang Q X and Smith M B 2005 Central brightening due to constructive interference with, without, and despite dielectric resonance *J. Magn. Reson. Imaging* **21** 192–6

[5] Ibrahim T S 2005 Analytical approach to the MR signal *Magn. Reson. Med.* **54** 677–82

[6] de Moortele V *et al* 2005 B_1 destructive interferences and spatial phase patterns at 7 T with a head transceiver array coil *Magn. Reson. Med.* **54** 1503–18

[7] Hoult D I and Lauterbur P C 1979 The sensitivity of the zeugmatographic experiment involving human samples *J. Magn. Reson.* **34** 425–33
[8] Nyquist H 1928 Thermal agitation of electric charge in conductors *Phys. Rev.* **32** 110
[9] https://en.wikipedia.org/wiki/Central_limit_theorem
[10] Edelstein W A, Glover G H, Hardy C J and Redington R W 1986 The intrinsic signal-to-noise ratio in NMR imaging *Magn. Reson. Med.* **3** 604–18
[11] Ocali O and Atalar E 1998 Ultimate intrinsic signal-to-noise ratio in MRI *Magn. Reson. Med.* **39** 462–73
[12] Wen H, Denison T J, Singerman R W and Balaban R S 1997 The intrinsic signal-to-noise ratio in human cardiac imaging at 1.5, 3, and 4 T *J. Magn. Reson.* **125** 65–71
[13] Collins C M and Smith M B 2001 Signal-to-noise ratio and absorbed power as functions of main magnetic field strength, and definition of '90°' RF pulse for the head in the birdcage coil *Magn. Reson. Med.* **45** 684–91
[14] Hoult D I 2000 Sensitivity and power deposition in a high-field imaging experiment *J. Magn. Reson. Imaging* **12** 46–67
[15] Lattanzi R, Sodickson D K, Grant A K and Zhu Y 2009 Electrodynamic constraints on homogeneity and radiofrequency power deposition in multiple coil excitations *Magn. Reson. Med.* **61** 315–34
[16] Cao Z, Sica C T, Oh S, McGarrity J, Horan T, Park B S and Collins C M 2010 An MRI simulator for effects of realistic field distributions and pulse sequences, including SAR and noise correlation for array coils *Proc. ISMRM (Stockholm)* p 1456
[17] Cao Z, Park J, Cho Z H and Collins C M 2015 Numerical evaluation of image homogeneity, signal-to-noise ratio, and specific absorption rate for human brain imaging at 1.5, 3, 7, 10.5, and 14 T in an 8-channel transmit/receive array *J. Magn. Reson. Imaging* **41** 1432–9
[18] Park B, Webb A G and Collins C M 2009 A method to separate conservative and magnetically induced electric fields in calculations for MRI and MRS in electrically small samples *J. Magn. Reson.* **199** 233–7
[19] Roemer P B, Edelstein W A, Hayes C E, Souza S P and Mueller O M 1990 The NMR phased array *Magn. Reson. Med.* **16** 192–225

IOP Concise Physics

Electromagnetics in Magnetic Resonance Imaging: Physical Principles, Related Applications, and Ongoing Developments

Christopher M Collins

Chapter 3

Fields and hardware for MRI

As described in the previous chapters, MRI typically requires three fundamentally different fields: the static magnetic B_0 field to induce nuclear alignment and precession, the RF magnetic B_1^+ field to excite nuclei to a state where they can produce a detectable signal, and the gradient fields G_x, G_y, and G_z, applied strategically through time to encode spatial information into the signal received from the spins. Also, by the principle of reciprocity, the sensitivity of each receive coil to signal from a given location is proportional to the strength of its B_1^- field at that location. Here we will discuss the basics of the requirements for these fields and of their associated hardware.

3.1 Static magnetic (B_0) fields

As mentioned previously, the strength of the net nuclear magnetization is proportional to the strength of the B_0 field. For this reason, it is desirable to have a very strong B_0 field. Today, B_0 field strengths for human imaging are typically on the order of tesla, with most standard hospital systems operating at 1.5 T or 3 T. There are numerous 7 T whole-body systems (e.g. [1–7]) and a handful of systems with even stronger fields (e.g. [8–10]) used throughout the world for research purposes. For comparison, the strength of the Earth's magnetic field is about 50 μT (or 0.00005 T) and the strength of a common refrigerator magnet is about 5 mT (or 0.005 T). Creation of homogeneous B_0 fields on the order of tesla over the entire imaging region requires strategic use of advanced technologies.

The vast majority of main magnets used today for human imaging rely on long, thin wires containing superconducting material wound into a specific pattern about a cylindrical bore to create a strong B_0 field along the axis of the cylinder. While this is the same principle on which a simple solenoidal coil is based, the windings of superconducting wire in an MRI magnet are not evenly spaced, but are wound into bands with thicknesses and positions chosen strategically to produce a homogeneous

doi:10.1088/978-1-6817-4083-6ch3

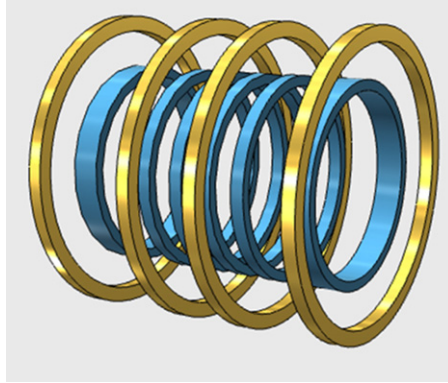

Figure 3.1. Conceptual diagram of bands of windings in a self-shielded B_0 magnet. Current flowing in the primary (blue) bands produces the desired B_0 field, while current flows in the outer bands in the opposite direction to help contain the magnetic flux of the system.

field at the center of the finite-length cylinder. Additionally, most magnets produced today are 'self-shielded', meaning that they contain superconducting windings with a larger diameter than the primary windings carrying current in the opposite direction of the primary windings. This helps to contain the magnetic flux to a smaller region for purposes of safety, and reduces the space (and associated cost) required to site an MRI system. Figure 3.1 shows a diagram indicating bands of wire in a self-shielded magnet design.

The superconducting material most often used is a niobium–titanium (NbTi) alloy having mechanical properties and cost of production making it suitable in production of large, strong magnets. The NbTi alloy is formed into filaments about 50 μm in diameter and a few hundred of these filaments are bundled and embedded into a copper matrix to form a composite wire between 0.5 mm and 1 mm in diameter.

Superconducting material can be characterized by its critical temperature, its critical magnetic field strength, and its critical electrical current. If the material experiences temperatures or fields or carries currents above the critical values it will come out of its superconducting state. These critical values are also related, such that a superconducting wire at a lower field strength and temperature can carry a greater current before coming out of its superconducting state than it would at a higher field strength or temperature. In practice, the operating temperature for almost all superconducting magnets is fixed at 4.2 K, the temperature of liquid helium. The superconducting windings are immersed in liquid helium within a 'dewar', which amounts to a specialized container for cryogens. A composite superconducting wire having a diameter of 0.6 mm might be able to carry about 500 A in a 3 T field before coming out of its superconducting state.

To obtain a simple first-order approximation of the length of wire required to create a 3 T magnetic field in a system for imaging the human body, we can use the well-known equation based on approximating the field strength inside a solenoid, $B = \mu nI/(\pi D)$ for a solenoid of diameter D with n turns of a wire carrying current I.

For $B = 3$ T, I = 500 A, $\mu = 4\pi \times 10^{-7}$ NA^{-2}, and $D = 1$ m, we find a number of turns, $n = 15000$, requiring over 45 km of wire for the primary windings alone.

The superconducting nature of these magnets means that the current will continue to circulate in the magnet indefinitely with no power required. Thus, the magnetic field is always present, even when the system is not being used.

To produce the greatest possible homogeneity of the B_0 field within the imaging region, a number of methods beyond the design of the superconducting windings described up to now are used. All of these methods are utilized in a process called 'shimming'. This name is most naturally related to the use of thin pieces of iron (iron shims) carefully positioned around the magnet bore. There are also a large number of 'shim coils', amounting to strategically wound wires carrying DC currents to maximize field homogeneity. These include superconducting shim coils immersed in the same helium dewar as the main B_0 windings, and 'resistive' (typically copper) shim coils that are slightly closer to the imaging region. Iron shims and superconducting shim coil currents are typically adjusted once for each MRI system, while resistive shim coil currents are adjusted for every new patient or imaging subject. The gradient coils described in the next section serve also as three of the resistive shim coils, where the DC currents to accomplish shimming are very small in comparison to the switched currents to accomplish spatial encoding.

3.2 Switched gradient magnetic fields

To encode spatial information onto the frequency and phase of the precessing nuclei, gradient coils are designed to produce linear field gradients through the imaging region. These gradient coils are located inside the static magnet and are typically enclosed behind the plastic casing which also covers the static magnet.

The simplest designs for this purpose are illustrated schematically in figure 3.2. As seen in the figure, creation of a field gradient in the z-direction can be as simple as using two loops with opposing currents. Creation of a transverse (x- or y-oriented) gradient, however, requires consideration of both the most effective currents in producing the gradient (near the center of the coil) and a current return path.

More advanced designs used today for z-gradient coils have many loops spaced strategically, and those for transverse coils include numerous loops in each 'quadrant' occupied by only one loop in the simple coil of figure 3.2. An example of transverse x- and y-gradient windings from simulation having eight loops in each quadrant of each coil is shown in figure 3.3.

Typically a single gradient coil (including all its loops in all four quadrants) is created from a single conductor such that all the loops in all the quadrants are connected in series. This ensures that the same current amplitude exists in all loops at any time, and allows for production of a strong field gradient with a single current source, but results in high inductance. This high inductance impedes rapid switching such that gradient amplifiers are necessarily very powerful. For a typical 3 T MRI system today, the gradient amplifier is capable of producing about 2 kV maximum voltage and 650 A maximum current. When driving a typical gradient coil this can produce a maximum field gradient of about 72 mT m^{-1} with a minimum rise time of 200 μs,

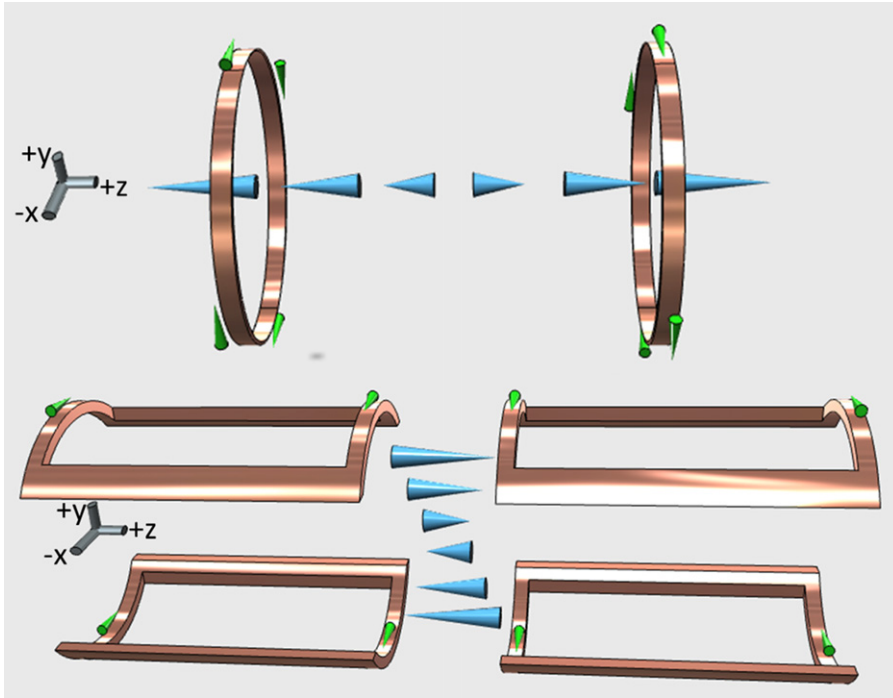

Figure 3.2. Conceptual illustration of a basic *z*-gradient coil (top) and a basic *y*-gradient coil (bottom). Directions of electrical currents are indicated with green darts, and magnetic field strength and orientations are indicated with blue darts. A basic *z*-gradient coil (top) consists of loops on opposite sides of the center of the imaging region carrying equal currents in opposite directions. A basic transverse gradient (bottom) has four quadrants with at least one loop in each where the loops carry currents such that the circumferential section nearest the center carries the currents (green darts pointing towards the reader in this illustration) primarily responsible for producing the desired gradient field.

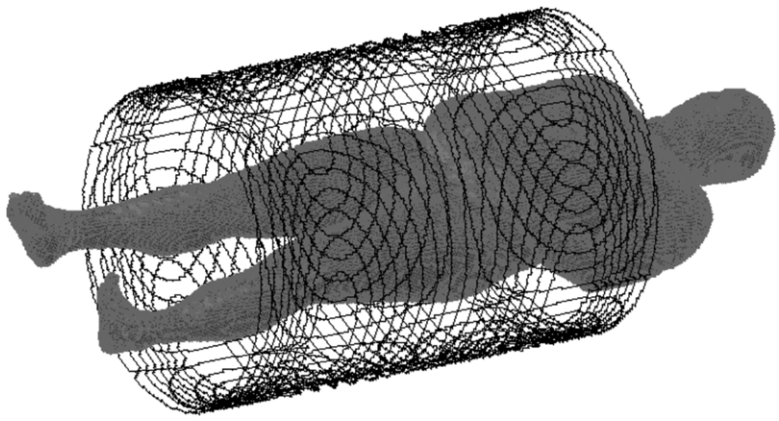

Figure 3.3. Model of human body in transverse (*x* and *y*) gradient coils with more modern windings, each coil having four symmetric quadrants and each quadrant having eight loops.

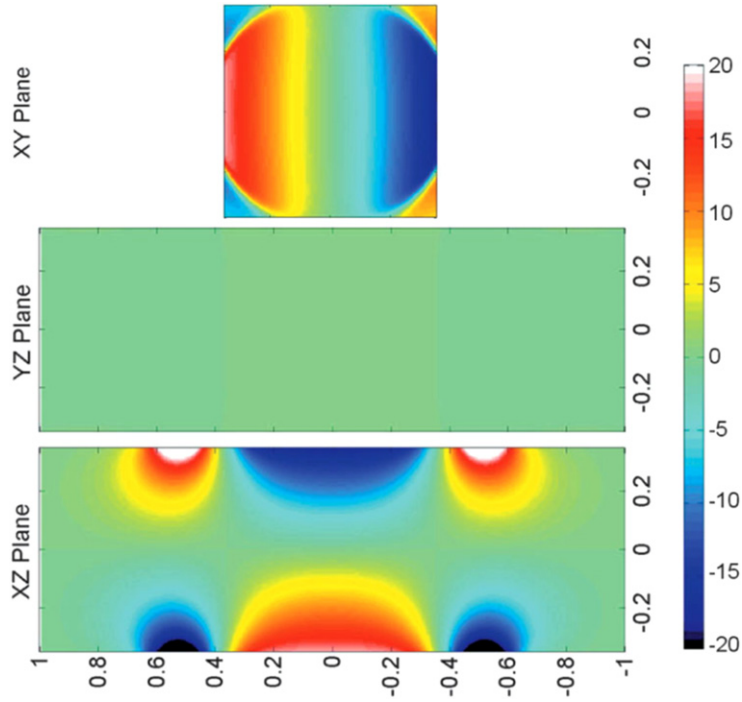

Figure 3.4. Distribution of *Bz* as produced by a transverse *x*-gradient coil like that in figure 3.3. Dimensions alongside each plot are in meters, and the dimensions of the color scale are in millitesla per kiloampere of current in the coil.

or a maximum slew rate of 345 T m^{-1} s^{-1}. The magnetic field distribution from a single *x*-gradient coil like that in figure 3.3 is shown in figure 3.4.

3.3 RF magnetic (B_1) fields

While the design and usage of RF coils has evolved significantly through the years and will continue to do so in the future, currently RF coils can be categorized generally into volume coils, surface coils, and coil arrays (which are typically arrays of surface coils). Most commonly in human imaging today, volume coils are used in transmission and arrays of surface coils are used in reception. Except for some very exotic coils used in research, all coils are constructed of metal (typically copper) conductors separated by lumped element capacitors to create an inductance–capacitance (LC) resonator with a desired current pattern having very low impedance at the Larmour frequency.

A volume coil is designed to produce a suitably homogeneous field over an imaging volume. In MRI today, the most commonly used volume coil is the body transmit coil, or system coil, which is integrated with the system and located behind the plastic casing which encapsulates the main magnet, shim coils, and gradient coils. The most common structure for the system body coil is the 'birdcage' structure [11], consisting of two loops called 'end rings' connected by a number of straight

conductors, called 'rungs' or 'struts'. Capacitors can be placed in the rungs to create a 'low-pass' birdcage coil, placed in the end rings to create a 'high-pass' birdcage coil, or placed in both the rungs and end rings to create a 'hybrid' birdcage coil. The names 'high-pass' and 'low-pass' come from the similarity of the structure, if unwrapped, to ladder-type LC filters.

From long before the invention of the birdcage coil, volume coils were designed based on the understanding that in the quasi-static regime an electrical current on a cylindrical surface oriented with the axis of the cylinder and having an amplitude varying with the sine of the azimuthal angle will produce a perfectly homogeneous field within the cylinder. Realizing that a current pattern similar to this could be created by wrapping a lumped-element transmission line one wavelength long into a cylindrical shape and connecting the two ends led to the invention of the birdcage coil [11]. The concept of the lumped element transmission line should be somewhat familiar to students of electromagnetics and communications, where the function of a transmission line is often described first in terms of two parallel inductive conductors (parallel wires or microstrip and backplate, etc) connected together periodically with capacitive bridges (representing the substrate or the material between the conductors). In a low-pass birdcage coil, the parallel conductors are the end rings and the capacitive bridges are the rungs.

Regardless of where the capacitors are placed, a birdcage coil is capable of supporting numerous resonances. The number of resonant modes is equal to $N/2$ for a low-pass birdcage coil and $N/2 + 1$ for a high-pass or hybrid birdcage coil, where the $N/2$ resonances arise from standing waves around the circumference of the coil (figure 3.5) and the additional mode in high-pass and hybrid coils arises from the fact that each end ring is itself an LC resonator. Upon close examination, many of these

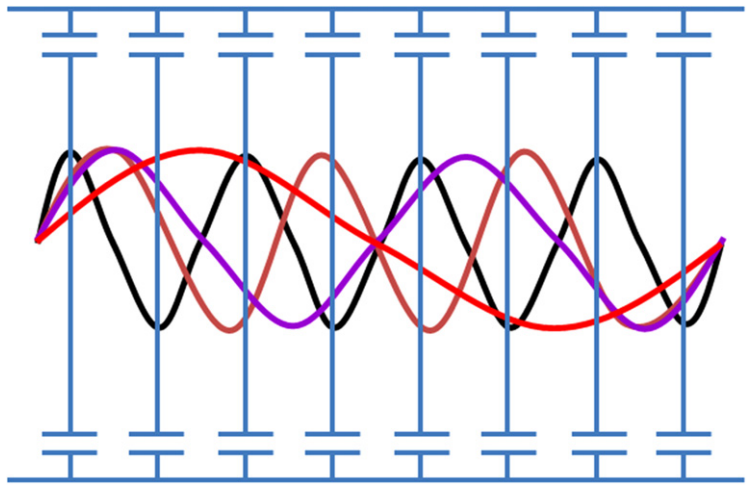

Figure 3.5. Modes supported in an eight-rung low-pass birdcage coil. Each colored line indicates current carried in the rungs (light blue) where it intersects them. The lowest mode, mode 1 (red line), results in one full cycle around the coil and is that used to produce a homogeneous field in MRI. The highest mode supported, mode 4 for an eight-rung birdcage coil (black line), results in opposite currents on adjacent legs.

modes are split due to slightly different frequencies of standing waves created from waves 'traveling' in opposite directions about the coil or, in the case of the end ring mode (often called 'mode 0'), slightly different frequencies of resonances with end ring currents being in the same or opposite directions from each other. It is only mode 1, with a full wavelength about the cylindrical birdcage, that creates a homogeneous field and is desired for operation of the system body coil. It is also the only mode producing a nonzero transverse field at the center of the coil. In a low-pass coil, mode 1 is expected to have the lowest resonant frequency with modes 2 to $N/2$ occurring at increasingly high frequencies. For a high-pass coil (and, by design, most hybrid coils) mode 0 is expected to occur at the highest frequency with mode 1 being the second highest and modes 2 to $N/2$ occurring at progressively lower frequencies. In practice, identifying mode 1 and tuning it to the desired frequency is accomplished with use of a spectrum analyzer, pick-up coils, and a combination of selecting the best fixed capacitors and adjusting tunable capacitors. The most effective locations for tuning capacitors is where currents in the coil are highest. Today almost all birdcage coils are high-pass or hybrid due to the difficulty in tuning mode 1 in a large low-pass coil to high frequencies. To ensure effective transmission of energy to the coil (ensuring both efficient system operation and avoiding reflection of power back towards the amplifier), matching circuits are also required to match the input impedance of the coil to the characteristic impedance of the coaxial transmission line, which is universally 50 ohms (Ω) in MRI.

While the birdcage coil is based on the idea of making the rung currents vary sinusoidally with the azimuthal angle, it is important to be aware that, due to Kirchoff's current law, the highest currents for any birdcage coil having eight or more rungs occur in the end rings (figure 3.6). The end ring currents also contribute to B_1 within the coil, but their contribution is not as well anticipated as that of the rungs.

Birdcage coils are typically driven in 'quadrature' to produce a circularly polarized field that interacts maximally with the precessing nuclei. A birdcage coil with a number of rungs that is evenly divisible by 4 will have a symmetry that allows it to be driven at two locations 90° apart from each other about the cylinder, such that each drive will be at a location where the currents of mode 1 from the other drive are at a minimum, and thus the two drives interact minimally with each other. If these two drives also have a 90° difference in phase, the result is a current pattern that rotates about the cylinder at the Larmour frequency producing a circularly polarized B_1 field at the center of the coil.

Figure 3.7 shows a photograph of a low-pass eight-rung birdcage coil built for imaging the knee. In this example, disc capacitors are placed across gaps at the center of each of the eight rungs. There are two feed points, 90° apart, to accomplish quadrature excitation for the production of circularly polarized fields. Variable capacitors at the feed locations accomplish matching to the 50 Ω source and additional variable capacitors in parallel to the disc capacitors immediately opposite the feed locations (not visible here) accomplish tuning to the desired frequency. During operation, the coil is placed inside the RF shield to ensure consistent operation and minimize any excitation and signal reception from the knee not being

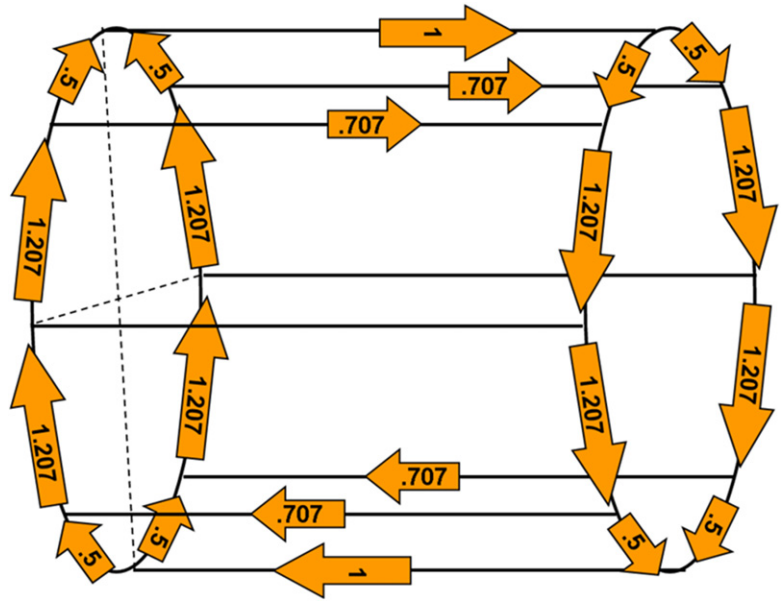

Figure 3.6. Instantaneous current in an eight-element birdcage coil, including end rings, in mode 1 resonance, with all currents normalized to the maximum rung current. At this instant, all currents would contribute to a magnetic field at the center of the coil that is oriented into the page, away from the reader.

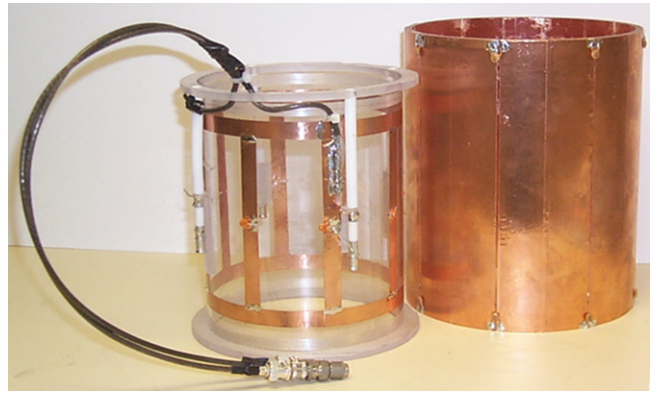

Figure 3.7. Experimental low-pass birdcage coil designed for imaging of the knee (left) beside its RF shield (right).

imaged. The shield is slotted with large-value capacitors across the gaps so to create a high-pass structure so that RF currents can pass (and RF fields will be shielded to remain in the imaging region), but low-frequency currents will be blocked (so that gradient fields will not be shielded from the imaging region).

Figure 3.8 shows a model of a human head inside a low-pass 12-rung birdcage coil with the cylindrical copper RF shield hidden for ease of visualization. The RF magnetic fields at different points in time on a transverse plane through the middle

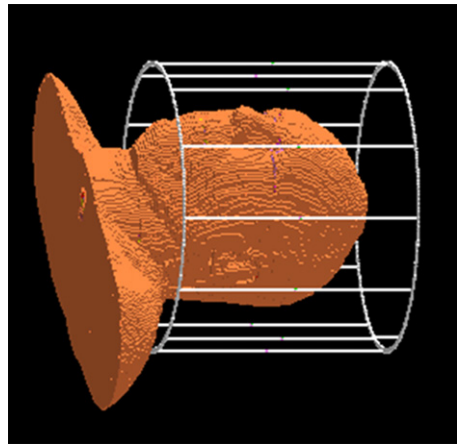

Figure 3.8. Model of a human head in a 12-rung low-pass birdcage coil.

of this coil resulting from driving this low-pass coil across only one capacitor in a rung near the back of the head (port 1), across only one capacitor located 90° away from port 1, in a rung near the side of the head (port 2), and of driving both of these ports with a 90° phase difference (in quadrature) at 64 MHz (as for a 1.5 T MRI system) are shown in figure 3.9. Figure 3.10 shows the resulting $|B_1^+|$ for all three cases. It is clear that the quadrature case has a stronger time-average field strength and also has a stronger $|B_1^+|$. In fact, if we can assume that at the center of the quadrature coil, $|B_y|$ is equal to $|B_x|$ and the 90° phase shift (in the proper direction) results in their maxima occurring exactly one quarter-cycle apart, the equations of (1.1) dictate that $|B_1^+|$ for the quadrature case should be exactly twice that of any port alone, while $|B_1^-|$ should be zero.

Note that in practice, ports 1 and 2 are typically located at +45° and –45° away from the back of the head rather than at the back and side, to ensure similar loading conditions seen from the two ports.

As evident in figure 3.10, although the electrical currents in the coil are symmetric about the x-axis (for port 1) or the y-axis (for port 2), the distribution of $|B_1^+|$ does not share this symmetry exactly, but is slightly stronger along a diagonal through the coil. For example, $|B_1^+|$ for port 2 is stronger in the upper right and lower left regions within the head than in the upper left and lower right regions. The reason for this is related to the induced eddy currents in the head, and also the fields related to these eddy currents, being out of phase with the currents in the coil. An illustration of this is given in figure 3.11.

According to Lenz's law, the electrical currents induced in the head will produce a magnetic field opposing change in the incident field. For this geometry, that means the currents in the head would lag those in the coil by about 90° of phase. As shown in the progression from the left frame to the right frame of figure 3.11, this results in a polarization that is primarily clockwise in the upper right and lower left regions, but counter-clockwise in the upper left and lower right regions.

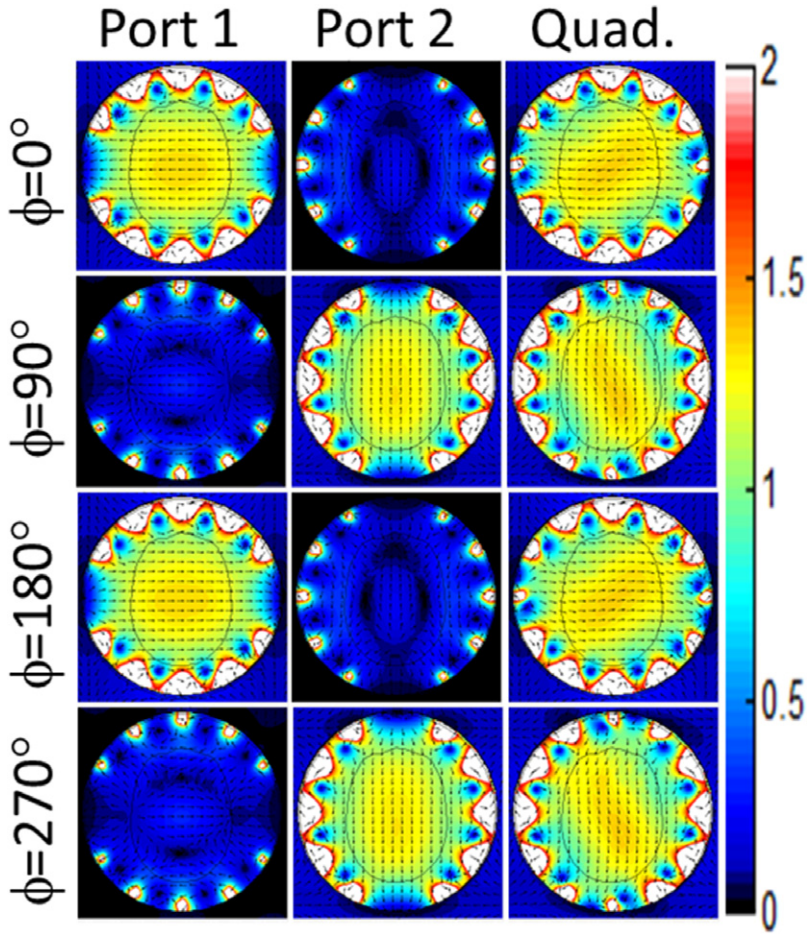

Figure 3.9. Instantaneous RF magnetic fields for birdcage coil model driven at either port and with both ports driven in quadrature. Here arrows indicate only the orientation of fields, while underlying color indicates its amplitude, with the units for the color scale in μT.

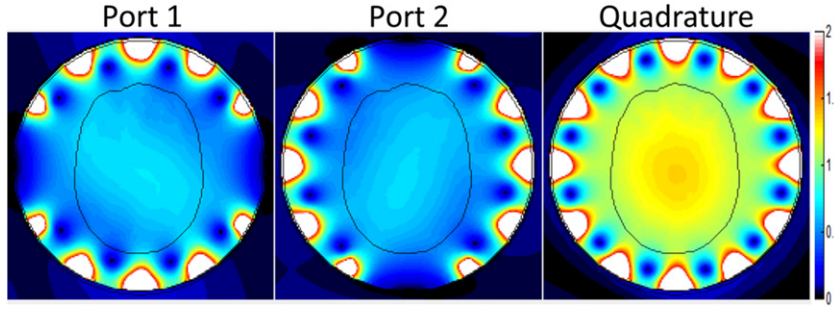

Figure 3.10. Distribution of $|B_1^+|$ on a mid-axial plane for a birdcage coil model driven at either port and with both driven in quadrature.

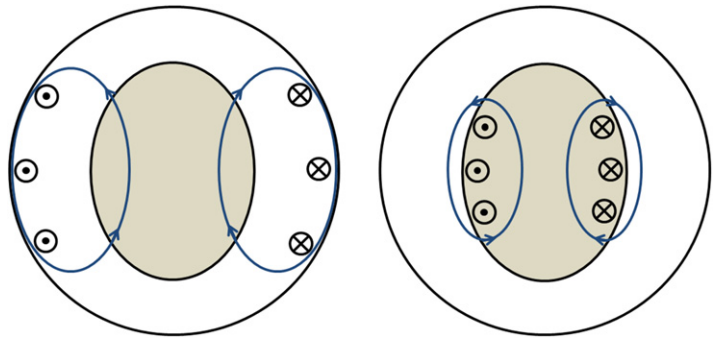

Figure 3.11. Illustration of the mechanism for asymmetry in circularly polarized field magnitude distributions despite symmetry in coil current distributions. Due to the phase difference between coil currents (left) and induced eddy currents in the sample (right), as well as their respective magnetic fields (indicated with blue arrows), the fields rotate in a predominantly clockwise direction at the upper right and lower left, and in a predominantly counter-clockwise direction at the upper left and lower right. Here the current and field orientations are as if driving at port 2 in simulations of figure 3.10. The shield location is indicated with the outer circle, the conductive tissue sample is indicated by the gray-shaded ellipse, and electrical currents oriented towards and away from the reader are indicated with small circles containing a dot and an 'x' respectively. The progression of the orientation of each blue arrow from the left frame (when coil currents are maximum) to the right (when eddy currents are maximum) indicates geometric asymmetry in dominant direction of polarization.

After nuclear excitation with the system body coil, encoding of spatial location, and other desired manipulations are finished so that signal is ready to be received, receive coils are used to detect the signal. In imaging of human subjects for medical purposes, the standard for reception is now multiple single-loop coils, or a coil array, with each coil positioned to receive strong signal from a different region of the body. Note that while in practice an array of N coils is often referred to as an 'N-channel coil', in this book the word 'array' is used to refer to cases where multiple coils are designed for simultaneous use. In fundamental acquisition, the signals from the different coils can then be combined in a variety of ways to produce a single image with strong signal throughout by a variety of methods, as discussed previously (section 2.5). Here we will briefly review the structure and electronics of receive arrays.

Each coil in a receive array is typically a single loop composed of multiple sections of metallic conductor separated by capacitors, resulting in an inductance–capacitance–resistance (LCR) resonant circuit designed to resonate at the Larmour frequency. Since receive coils are not driven, matching of the coils themselves is not critical and often low-impedance preamplifiers positioned very near each coil are used to ensure effective transmission of signal from the coil to the system spectrometer. In order to ensure that the receive coils and their sensitive electronics are not damaged by strong induced currents during excitation with the system body coil, it is important to ensure that they are detuned during transmission. To ensure the currents in each coil are induced only by nuclei in the body and not by currents in adjacent coils it is important to decouple receive coils from each other.

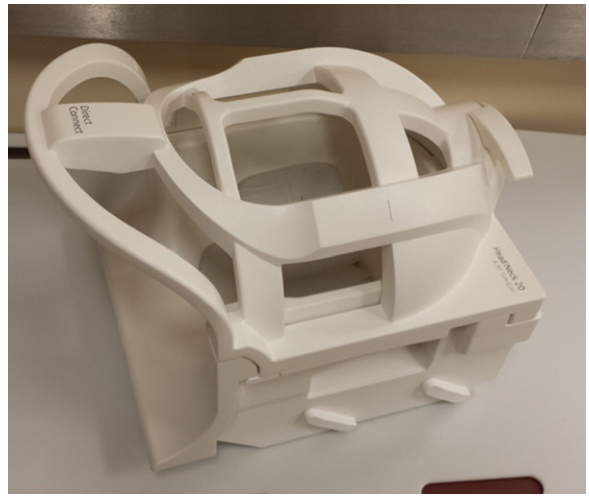

Figure 3.12. A 20-channel commercially manufactured receive array coil for clinical imaging of the head and neck.

Receive coils can be detuned during transmission by a number of methods, including passive and active detuning circuits. A passive detuning circuit can be as simple as two diodes oriented in opposite directions both placed in parallel to one of the capacitors in the coil. With this arrangement, large induced currents flowing in either direction, as caused by the transmit coil, will forward-bias the diodes and bypass the capacitor, such that the coil is no longer resonant at the Larmour frequency. An active detuning circuit can involve diodes between some point in the coil and ground so that when an active DC bias voltage is present, large induced currents will be shunted away from any sensitive electronics.

Receive coils can be effectively decoupled from adjacent receive coils by strategically overlapping them so that the mutual inductance between them is zero. For circular coils each of diameter D, for example, this amount of overlap occurs when the distance between the coil centers is about $0.78D$ [12]. It is also possible to use a variety of circuits to accomplish decoupling of coils [13].

Use of an RF coil array allows for each individual RF coil to be positioned to optimize reception of signal from a different portion of the body. Thus, the geometry of an array will depend largely on the portion of the body the entire array is designed to image. Figure 3.12 shows an example of a commercially manufactured head and neck array containing 20 loop coils. Most modern MR systems for imaging humans have an array for imaging the posterior (back) side of the body that can be placed within the patient bed and a wide variety of portable coil arrays available for imaging different portions of the body.

References

[1] Vaughan J T *et al* 2001 7 T vs 4 T: RF power, homogeneity, and signal-to-noise comparison in head images *Magn. Reson. Med.* **46** 24–30

[2] Brunner D O, De Zanche N, Fröhlich J, Paska J and Pruessmann K P 2009 Travelling-wave nuclear magnetic resonance *Nature* **457** 994–8
[3] Hong S M, Park J H, Woo M K, Kim Y B and Cho Z H 2014 New design concept of monopole antenna array for UHF 7 T MRI *Magn. Reson. Med.* **71** 1944–52
[4] Teeuwisse W M, Brink W M and Webb A G 2012 Quantitative assessment of the effects of high-permittivity pads in 7 tesla MRI of the brain *Magn. Reson. Med.* **67** 1285–93
[5] Zelinski A C, Angelone L M, Goyal V K, Bonmassar G, Adalsteinsson E and Wald L L 2008 Specific absorption rate studies of the parallel transmission of inner-volume excitations at 7 T *J. Magn. Reson. Imaging* **28** 1005–18
[6] Sigmund E E, Suero G A, Hu C, McGorty K, Sodickson D K, Wiggins G C and Helpern J A 2012 High-resolution human cervical spinal cord imaging at 7 T *NMR Biomed.* **25** 891–9
[7] van den Bergen B, van den Berg C A, Klomp D W and Lagendijk J J 2009 SAR and power implications of different RF shimming strategies in the pelvis for 7 T MRI *J. Magn. Reson. Imaging* **30** 194–202
[8] Vaughan T *et al* 2006 9.4 T human MRI: preliminary results *Magn. Reson. Med.* **56** 1274–82
[9] Shajan G, Kozlov M, Hoffmann J, Turner R, Scheffler K and Pohmann R 2014 A 16-channel dual-row transmit array in combination with a 31-element receive array for human brain imaging at 9.4 T *Magn. Reson. Med.* **71** 870–9
[10] Atkinson I C, Renteria L, Burd H, Pliskin N H and Thulborn K R 2007 Safety of human MRI at static fields above the FDA 8 T guideline: sodium imaging at 9.4 T does not affect vital signs or cognitive ability *J. Magn. Reson. Imaging* **26** 1222–7
[11] Hayes C E, Edelstein W A, Schenck J F, Mueller O M and Eash M 1985 An efficient, highly homogeneous radiofrequency coil for whole-body NMR imaging at 1.5 T *J. Magn. Reson.* **63** 622–8
[12] Roemer P B, Edelstein W A, Hayes C E, Souza S P and Mueller O M 1990 The NMR phased array *Magn. Reson. Med.* **16** 192–225
[13] Lee R F, Giaquinto R O and Hardy C J 2002 Coupling and decoupling theory and its application to the MRI phased array *Magn. Reson. Med.* **48** 203–13

IOP Concise Physics

Electromagnetics in Magnetic Resonance Imaging: Physical Principles, Related Applications, and Ongoing Developments

Christopher M Collins

Chapter 4

Tissue/field interactions, MRI safety, and field-related image artifacts

While the magnetic fields applied interact with the spins in ways required to accomplish MRI, they interact with tissue and other materials in a number of additional ways that can both have implications for safety and affect the images produced. Here we survey the most important of these interactions and their effects.

4.1 Interactions between fields in MRI and biological tissue

A good place to start understanding the various interactions of electromagnetic fields with tissues is with consideration of the material properties in the Maxwell equations, ε, σ, and μ. These measureable properties arise directly from the most significant interactions between the fields and the tissues (table 4.1).

First, consider magnetic permeability, $\mu = \mu_r\mu_0$. In general, common materials can be classified into three categories with regards to their magnetic permeability: diamagnetic (with μ_r slightly less than 1), paramagnetic (with μ_r slightly greater than 1), and ferromagnetic (with μ_r much greater than 1). In general, tissues tend to be slightly diamagnetic while air tends to be slightly paramagnetic (table 4.2). Modern MR-conditional metallic implants also tend to be paramagnetic, and ferromagnetic materials should generally not be taken near an MRI system for reasons of safety, as will be discussed later (section 4.2).

The mechanisms by which materials can be paramagnetic and ferromagnetic are understood relatively easily, as the majority of unpaired proton spins, electron spins, and electron orbits will be in their lower possible energy states, and thus produce magnetic moments that are aligned with the applied magnetic field resulting in a magnetic flux density that is larger within the material than it would be in a vacuum.

The mechanism by which materials can be diamagnetic requires a little more thought, but can be understood intuitively by considering a pair of electron orbits in a

doi:10.1088/978-1-6817-4083-6ch4

Table 4.1. The Maxwell equations.

	Differential form	Integral form
Gauss's law	$\nabla \cdot \varepsilon \mathbf{E} = \rho_v$	$\oiint_s \varepsilon \mathbf{E} \cdot d\mathbf{s} = \iiint_v \rho_v dv$
Gauss's law for magnetism	$\nabla \cdot \mathbf{B} = 0$	$\oiint_s \mathbf{B} \cdot d\mathbf{s} = 0$
Faraday's law	$\nabla \times \mathbf{E} = -\frac{\partial}{\partial t}\mathbf{B}$	$\oint_l \mathbf{E} \cdot d\mathbf{l} = -\iint_s \frac{\partial}{\partial t}\mathbf{B} \cdot d\mathbf{s}$
Ampere's law with Maxwell's addition	$\nabla \times \frac{1}{\mu}\mathbf{B} = (\sigma \mathbf{E} + \frac{\partial}{\partial t}\varepsilon \mathbf{E})$	$\oint_l \frac{1}{\boldsymbol{\mu}}\mathbf{B} \cdot d\mathbf{l} = (\iint_s \sigma \mathbf{E} \cdot d\mathbf{s} + \iint_s \frac{\partial}{\partial t}\varepsilon \mathbf{E} \cdot d\mathbf{s})$

Table 4.2. Relative magnetic permeability of select tissues [1].

Material	μ_r
Free space	1.00000000
Air	1.00000040
Water	0.99999096
Fat	0.99999221
Bone	0.99999156
Blood	0.99999153
Gray matter	0.99999103
White matter	0.99999120

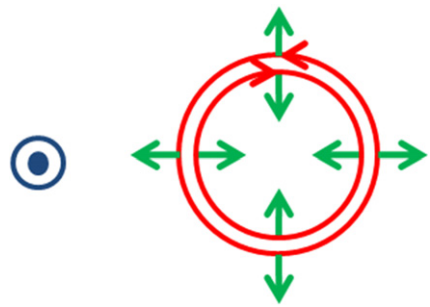

Figure 4.1. A pair of electron orbits (red arrows in direction of electric current, opposite to direction of electron travel) in a magnetic field oriented toward the reader (blue) and the forces experienced by the orbits. In this illustration, the orbit producing clockwise current will be 'accelerated' while the orbit producing counter-clockwise current is 'decelerated'. The result is a net current in the clockwise direction, creating a field which opposes the original field.

situation where all proton spins, electron spins, and electron orbits are paired. Such a situation is illustrated in figure 4.1 for a pair of electron orbits in the presence of a magnetic field oriented out of the page [2]. Here the electron orbits producing clockwise and counter-clockwise electrical currents are drawn as being circular and having different radii for ease of visualization, not because they are actually circular or

expected to have different radii. Also, the direction of the arrows on the orbits indicates the direction of electrical current, which is opposite the direction of electron travel.

With the relationship $F = qv \times B$ it is possible to calculate the forces experienced at different locations on these two orbits. The orbit with a clockwise current will generally experience a force towards its center, in effect accelerating it and increasing the effective current within it while that with a current flowing in the counter-clockwise direction will experience forces away from its center which thus decelerate it, reducing its effective current. The net field produced by these two orbits will thus have a direction that opposes that of the applied field, resulting in a magnetic flux density that is slightly lower than that which would be experienced in a vacuum.

Since the differences in magnetic susceptibility between tissues are so small, it requires application of a strong field for a relatively long time for their effects to become notable. In practice, the effects of magnetic susceptibility in MRI are only appreciable for the B_0 fields, as they are very strong and applied continuously during the imaging period.

Now we consider electric conductivity σ and electric permittivity $\varepsilon = \varepsilon_r\varepsilon_0$ of tissues. Although in MRI we are generally only interested in applying magnetic fields to manipulate the tissue magnetization vector as according to the Bloch equation, as apparent in the Maxwell equations, every time-varying magnetic field is associated with an electric field. The electrical properties of tissue are thus pertinent to the gradient and RF fields of MRI.

In a water-based conductive fluid at frequencies below the microwave regime, electrical conductivity is determined primarily by salinity (the concentration of ions in the fluid) and electrical permittivity is determined primarily by the polarization field resulting from the alignment of dipolar water molecules with the applied electric field [3]. In semisolid fat (or even liquid oils) and solid cortical bone, relatively little translation of ions or rotation of dipoles can occur in response to an applied electric field, and σ and ε_r are, consequentially, relatively low [3].

In most biological tissues, the compartmentalization of conductive fluids into extracellular and intracellular spaces separated by lipid-based (fatty) cell membranes results in a situation where electric permittivity and conductivity are somewhat coupled and are frequency-dependent. Consider spaces as illustrated in figure 4.2, top, in the presence of an applied alternating electrical field. At a low frequency, there is a slight translation of ions in the fluid such that a polarization field is set up. At a low frequency, the ions spend little time in motion compared to that producing the polarization field so that the behavior of the bulk tissue results in low conductivity and high permittivity. Above some critical frequency, however, the motion of the ions can no longer keep up with the rapid field oscillations, and thus the ions spend more time in motion and are not able to set up the polarization field as effectively as at the lower frequency. The result is a higher conductivity and lower permittivity than seen at the lower frequency [3].

The mechanism just discussed is known as ‘interfacial polarization’ and is one of several mechanisms that contribute to the ‘dispersive’ nature of tissues [3]. A dispersive material has frequency-dependent electrical properties, much as a prism, which has the ability to disperse light according to its frequency and color. In

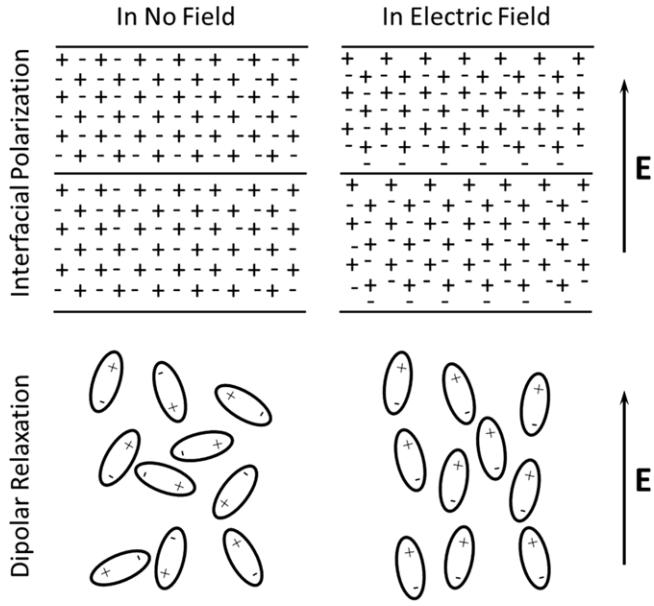

Figure 4.2. Two mechanisms of interaction between electric fields and tissue.

tissues, the mechanism of membrane polarization results in what is known as the beta dispersion. The critical frequency for the beta dispersion depends greatly on the organization of membranes in the tissue, and thus on the tissue of interest and, in cases of elongated structures such as muscle tissue, on the orientation of the fields in the tissue [3]. Nonetheless, the critical frequency of the beta dispersion is generally in the low MHz regime such that we can expect tissue orientation to have little effect on bulk tissue electrical properties at frequencies used commonly in MRI today.

There are also some other established dispersive mechanisms, one of which is the rotation of water dipoles with an applied electric field, resulting in the gamma dispersion [3], which occurs in the low GHz regime, as illustrated in figure 4.2, bottom. Briefly, at a low frequency the dipolar water molecules become aligned with the electric field spending little time of each cycle in rotation such that permittivity is high and conductivity is low. Above some critical frequency, the rotation of the dipoles can no longer keep up with the field oscillations to that they spend more time of each cycle in rotation and less aligned with the field, resulting in an increase in conductivity and a decrease in permittivity.

Figure 4.3 shows the electrical properties for transverse muscle tissue [4] with some of the dispersion regions labeled. Currently, MRI systems tend to operate between the beta and gamma dispersions. Figure 4.4 shows the electrical properties of several tissues in this regime [4]. The increase in conductivity of the gamma dispersion results in a severe shortening of field penetration depths and will probably prohibit effective MRI in humans at frequencies above the low GHz regime, even if other current technologic limitations, such as the creation of B_0 fields of, say, 50 T over the human body, are overcome.

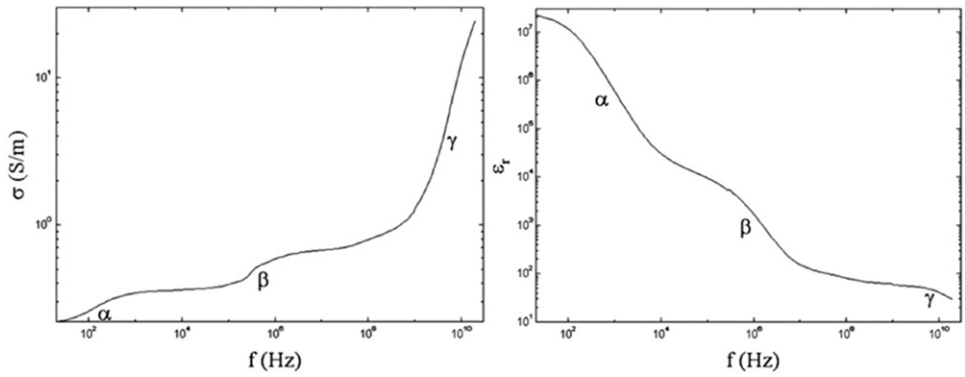

Figure 4.3. Electrical properties of muscle tissue over a frequency range showing some known dispersion regions.

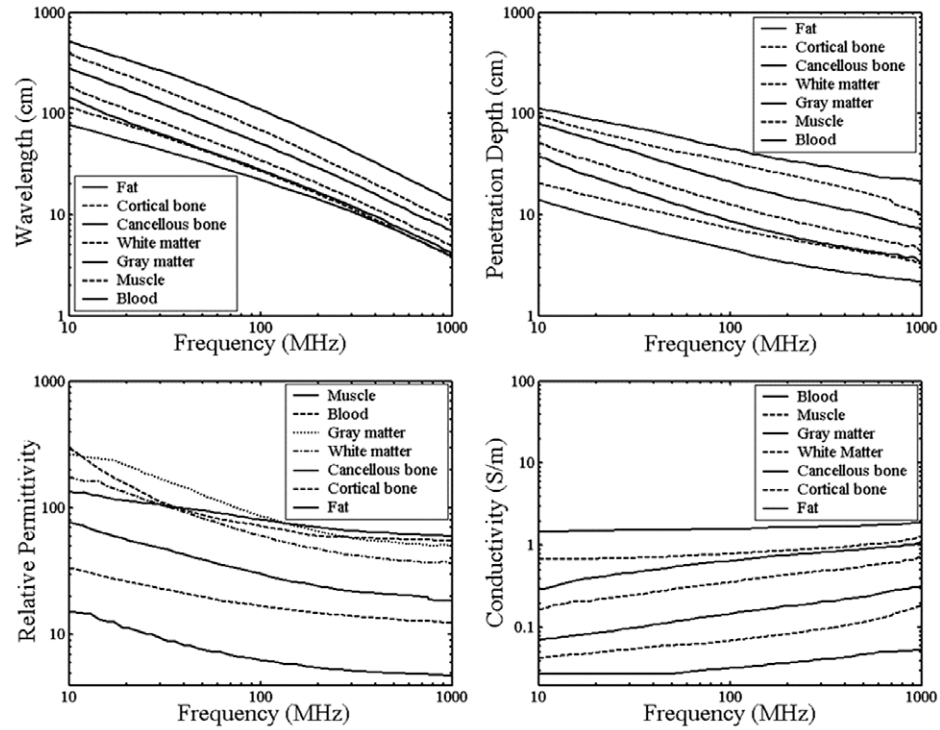

Figure 4.4. Electrical properties of several tissues over the frequency range pertinent to MRI in humans today. In each plot, the order of lines in the legend, from top to bottom, is the same as that for the lines in the plot at the high end of the frequency range shown.

4.2 Interactions between fields in MRI and ferromagnetic and conductive materials

As MRI has become an increasingly important component of the standard of care for a large number of medical cases, there is a growing expectation that patients with

active and passive medical devices implanted in their bodies should be able to benefit from it. Additionally, a number of medical procedures, from measuring an electrocardiogram in a patient to using localized RF ablation during MRI, require insertion of materials besides the human subject and the MRI receive coils into the MRI system. Notably, there have been major injuries and even death in MRI caused by ferromagnetic or conductive materials being brought into the system either with or without the knowledge of the system operators. Besides the issue of safety, foreign materials can affect the fields in MRI enough to severely distort the final images. It is thus important to understand the interactions between the MRI system that can result in harm in order to avoid injury by engineering of the devices in question, careful operation of the machinery, and/or avoiding any MR imaging of the patient with the implant altogether.

Ferromagnetic objects can experience both translation and rotational forces in the strong static (B_0) fields used in MRI many times the force of gravity. This can result in trauma to tissues from forces on passive or active implants within the body (for example, tearing of arteries due to forces on stents), or malfunction of active implants (for example, the closing or opening of a switch in a pacemaker). Additionally, ferromagnetic, and even paramagnetic objects can have very strong effects on the magnetic fields in MRI, resulting in severe distortions of the images.

Any conductive object can have electrical currents induced within it by the time-varying fields used in MRI. This can result in localized burns to tissue and, depending on the location of the burn, severe injury or even death. Even if safety is assured, these strong currents can cause distortions of the MR images, such as due to regions of very weak B_1 fields.

Increasingly, both passive and active implants are being designed with MRI in mind, and (for example) they are now much more likely to be made with materials such as titanium or low-susceptibility stainless steel than in previous years. Conductive leads are increasingly designed with wire windings designed to impede high-frequency currents induced by gradient and RF fields in MRI while allowing the extremely low-frequency pulses needed for performance. Also, implant manufacturers are increasingly devoted to carefully evaluating their products to determine under what conditions their recipients can be imaged safely.

4.3 Safety and biological effects of static, switched, and RF magnetic fields in MRI

By far, the greatest potential danger of an MRI system in routine operation is that posed by materials not known to be safe (or at least 'conditionally safe') in the MRI environment making it into the MRI suite and/or magnet room. This can include any ferromagnetic object, from an oxygen tank to a patient gurney, screwdriver, paper clip, or pen, which—if brought close enough to the system—can experience forces many times the force of gravity, making the object become a projectile and potentially causing injury or even death. Similarly, a ferromagnetic implant in a patient or anyone else approaching the MRI system could experience forces resulting in serious internal injury or death. Even miniscule shavings of

metal in the eyes of machinists have been known to cause serious damage to the eyes of the subject. Non-ferrous conductive materials inside or in contact with the human body can carry large electrical currents induced by the time-varying (gradient and RF) fields potentially leading to local tissue burns or nerve stimulation deep in the body.

Increasingly, implants and hospital equipment are designed to be 'MR safe' (safe in the MRI environment regardless of the part of the body being imaged, field strength, RF coils, or pulse sequence used) or at least 'MR conditional' such that under certain circumstances they can be present in the MRI environment.

Given the grave potential danger that foreign objects pose in the MRI environment, the most valuable component to ensuring safety is a diligent staff that rigorously screens all patients and anyone else entering the magnet room. Databases are available indicating what implants can be present in the MR environment under what circumstances [5], as are recommendations for screening procedures and what persons should be allowed in what areas surrounding an MRI system [6]. Staff should not allow anyone near the MRI system who has not been carefully screened, both physically and with questionnaires about medical history, body modifications (including piercings and tattoos), and even occupational history, as (again) some metal workers have experienced eye injuries in MRI due to previously unknown iron filings lodged in their eyes. All jewelry should be removed, and many sites will insist anyone entering the MRI suite remove their street clothes and wear only gowns provided by the institution. Subjects undergoing MRI are also instructed to wear ear protection and are in contact with the staff throughout the procedure so that they can easily report any issues. Subjects under anesthesia (often young children) require extra precautions and monitoring on the part of the staff, as they cannot report unusual sensations. Signage and physical barriers should also prevent anyone from entering the area without permission from the staff. At many sites metal detectors are used as a supplementary tool in ensuring safety.

In the absence of any ferromagnetic objects, some non-hazardous biological effects of the B_0 field are possible. The two most commonly reported are a sense of vertigo (sometimes described as dizziness or seasickness) and a metallic taste on the tongue, both resulting from motion in the B_0 field. The sense of vertigo arises from the fact that fluid in the inner ear that is ordinarily pulled towards the earth by gravity experiences other forces when the head is moving in a strong magnetic field. Because the fluid is electrically conductive, motion in a magnetic field produces forces other than gravity that confuse the senses as to which way is up, resulting in a slight loss of balance and a general sense of vertigo or seasickness. The metallic taste on the tongue arises from motion in the B_0 field inducing electrical currents across the conductive surface of the tongue. The nerve endings on the very surface of the tongue can be stimulated by these electrical currents. Note that neither of these biological effects pose any long-term threats, and are not considered issues with respect to MR safety, but are known biological effects of the B_0 field in MRI. Nonetheless, these sensations can be unpleasant and are best to avoid when possible. To avoid the sensations of vertigo and metallic taste in patients, whenever possible

patient positioning on the patient table is performed with the head as far from the strong B_0 fields as possible, and the patient table is then moved carefully into the main magnet with controlled motion.

In ordinary operation, and in the absence of foreign implants or other materials, the greatest safety concern of the gradient fields is not due to direct interaction of fields with tissues, but due to the acoustic noise resulting from the very large forces caused by pulsing the gradient coils in the presence of the very strong B_0 field. This acoustic noise can be extremely loud, and as B_0 field strengths increase and gradient amplifiers become more powerful, more effort is required to minimize the vibrations causing acoustic noise. The US FDA recommends a limit of 140 dBA in the empty bore, but even when systems are operated well below these levels patients are required to wear hearing protection, in the form of either earplugs or a protective headset to avoid discomfort and hearing damage.

An occasionally reported, non-hazardous biological effect of the switched gradient fields is peripheral nerve stimulation (PNS). Under certain conditions, the gradient fields are capable of stimulating nerves on the outer surface of the body. This occurs by way of the electrical currents induced in the body by the time-varying gradient fields. The nerves stimulated can be either sensory neurons or motor neurons. If sensory neurons are stimulated, a sense of pressure at a certain location in synchronization with the pulsing (and acoustic noise) of the gradient field is most often reported. If motor neurons are stimulated, the twitching of a muscle in a certain region in synchronization with the pulsing of the gradient coils occurs. PNS can be uncomfortable, but is transient with no effects after the end of the imaging sequence. In principle, it is possible to stimulate deeper nerves, including those controlling heartbeat and respiration, however, long before deeper nerves are stimulated, severe pain and muscle contraction at the surface of the body would be apparent. To avoid discomfort from PNS, various limits have been recommended regarding what type of gradient switching rates are allowable under normal operation. Some define a limitation on maximum rate of change of the field (dB/dt) anywhere in the subject [7], or on patient sensation itself [8]. Other physiologically relevant limits have been proposed [9].

The RF fields in MRI can cause heating of tissues even in the absence of conductive implants or other materials in contact with the body. This can result either in whole-body heating to levels of discomfort or even thermoregulatory distress, or in local heating which, in extreme cases, can result in local tissue burns. It is not uncommon for subjects to report feeling warm during an MRI procedure, but this can be due to many factors, including the use of blankets to avoid the commonly reported sensation of feeling cold in the MRI suite.

To avoid dangerous levels of RF heating, MR systems are designed incorporating methods for limiting the RF energy absorbed by the subject, or the specific energy absorption rate (SAR, units of watts of RF power divided by kilograms of tissue) over some time period. The rate of energy absorption into the entire subject, or the whole-body SAR (SAR_{WB}), can be estimated as the difference between the power transmitted to the excitation coil and that reflected by the coil multiplied by an estimate of the percent of power received by the coil that is absorbed in the subject

(often determined with experimentally measured quality factors with the coil loaded and unloaded) divided by the mass of the body

$$\mathrm{SAR_{WB}} \approx \frac{(P_{\mathrm{forward}} - P_{\mathrm{reflected}})\left(1 - \dfrac{Q_{\mathrm{loaded}}}{Q_{\mathrm{unloaded}}}\right)}{\text{Patient mass}}.$$

Commonly, $\mathrm{SAR_{WB}}$ is limited to 2 W $\mathrm{kg^{-1}}$ over any 6 min period in clinical MRI exams [7]. In the case where a head-only transmit coil is used, the SAR over the head ($\mathrm{SAR_H}$) can be limited with a similar procedure, dividing the estimated power absorbed by the head by the approximate mass of the head. $\mathrm{SAR_H}$ is often limited to about 3 W $\mathrm{kg^{-1}}$ over any 6 min period in clinical MRI exams [7]. With a similar approach [7], a partial-body SAR ($\mathrm{SAR_{PB}}$) can be defined to limit heating due to other volume transmit coils used to excite a particular part of the anatomy, such as a wide variety of coils for imaging the extremities (knee, wrist, etc).

The limitation of RF energy to avoid local RF burns requires different methods. Specific recommended limits on the SAR in any 10 g ($\mathrm{SAR_{10g}}$) are commonly cited [7]. Right now estimates of $\mathrm{SAR_{10g}}$ are most often made with numerical simulations using models of human anatomy [10]. Although the geometry of these models does not generally match the anatomy of the subject being imaged [11], it is possible to ensure conservative estimates of SAR to ensure safety [12, 13]. The maximum $\mathrm{SAR_{10g}}$ during an MRI exam can then be estimated by either multiplying the real-time measured volume SAR pertinent to the coil being used ($\mathrm{SAR_{WB}}$, $\mathrm{SAR_H}$, or $\mathrm{SAR_{PB}}$, as appropriate) by a ratio of the simulated maximum $\mathrm{SAR_{10g}}$ to the corresponding simulated volume SAR. Due to the strong dependence of SAR distribution on subject geometry, suitable safety factors must be used in order to ensure local SAR levels are not excessively high in the subject.

Because SAR by itself can have little relation to temperature through time, there are increasing efforts to both predict and regulate temperature through time [14–16]. Simulation of temperature throughout the human body requires consideration of thermal equations in addition to the Maxwell equations, including consideration of the effects of perfusion by blood and other physiological phenomena.

4.4 Some field-related image artifacts in MRI and basic methods for their reduction

As described up to now, the ideal situation in the imaging region for conventional MRI would include a perfectly homogeneous B_0 field, perfectly linear gradient fields, a perfectly homogeneous B_1^+ field and high transmit efficiency of the transmit coil, and high sensitivity ($B_1^-/\sqrt{P}$) of the receive coil(s). Generally, unwanted distortions of MR images are referred to as 'artifacts', and they have a large number of sources, including motion, flow, and even Gibbs ringing from use of a low resolution image matrix in imaging an object with high signal contrast and sharp borders. While there are a number of ways to correct for these various imperfections or avoid them altogether [17], in this section we will explore how images affected by non-ideal field distributions can appear if uncorrected.

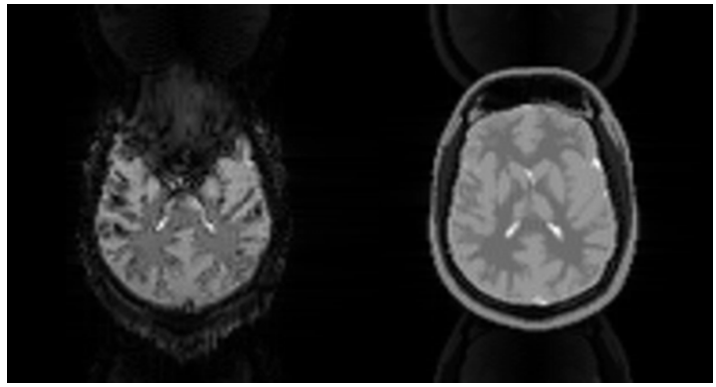

Figure 4.5. Mis-mapping in gradient echo EPI (left) is less prominent when a spin echo is present (right).

An inhomogeneous B_0 field can result in two broad types of image artifacts: mis-mapping and signal loss.

Mis-mapping occurs when nuclear precession at a given location is affected by the deviation from the anticipated B_0 field (ΔB_0) so much that it precesses at a frequency corresponding to a different location when the frequency-encoding gradient is applied and the signal is acquired. Thus, mis-mapping occurs in the frequency-encoding direction. Because absolute signal phase is known to be affected by numerous factors, phase encoding with multiple repetitions each having different strengths of the phase-encoding gradient ensures that B_0 inhomogeneity does not affect mapping in that direction. Figure 4.5 shows a simulated example of mis-mapping in a particularly sensitive sequence, a Cartesian gradient-echo EPI sequence. Effects of mis-mapping can be reduced with use of strong read-out (frequency-encoding) gradients. Stronger read-out gradients also result in shorter signal acquisition times and, consequently, higher receive bandwidths and greater noise.

Signal loss can occur when the B_0 inhomogeneity across a single voxel is great enough that the resulting dephasing causes significant decay of the signal from that voxel. As mentioned previously, this dephasing due to B_0 inhomogeneity is one of the contributors to T_2^* decay and generally can be reversed with the use of spin echoes. In cases where sensitivity to local tissue susceptibility effects are desired for signal contrast, however [18, 19], use of a spin echo sequence may not be desirable. Figure 4.6 shows a simulated example of signal decay due to B_0 inhomogeneity in a gradient echo sequence and absence of this signal loss with use of a spin echo sequence.

Deviations from a linear relationship between location and the strength of the gradient field applied in any direction result in mis-mapping of signal along that direction. In fact, no gradient field is perfectly linear in MRI, and slight inaccuracies in geometric representation are sometimes considered a limitation of MRI in comparison to x-ray based CT. Of course, MRI has many advantages over CT in many cases, and fortunately the nonlinearities in the gradient fields are not subject dependent, such that once they have been characterized it is possible to implement post-processing algorithms to correct the images and minimize their effects on all patients. Figure 4.7 shows a simulated example of uncorrected image distortion due to imaging in

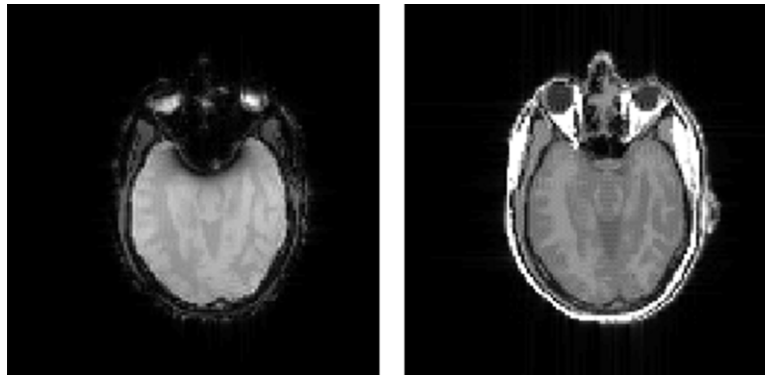

Figure 4.6. Signal loss due to B_0 inhomogeneity in a gradient echo sequence with long TE and TR (left) compared to a spin echo image with short TE and TR having no noticeable effects from B_0 inhomogeneity (right).

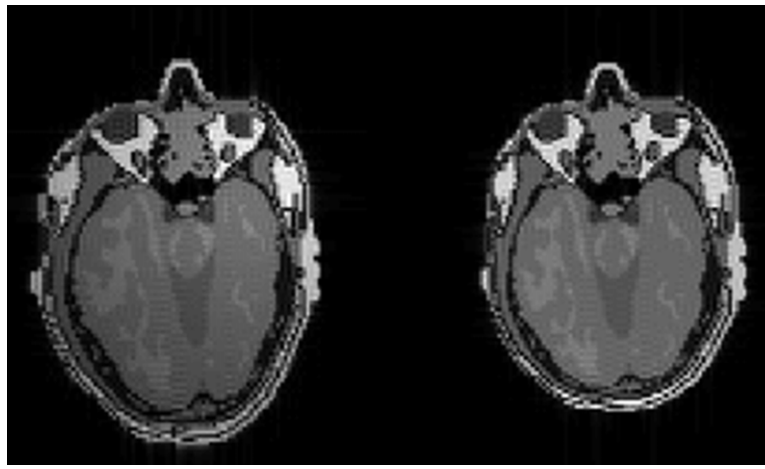

Figure 4.7. Geometric distortion due to gradient nonlinearities far from the center of the gradient coils (left) compared to an image acquired at the center of the coils (right).

a region of the gradient coils far from the center of the magnet, where the fields are less linear.

An inhomogeneous excitation field B_1^+ can cause undesired variations in both signal intensity and contrast throughout the image. It is easy to understand why inhomogeneous excitation would result in inhomogeneous signal intensity by remembering that the detected signal at any one location is proportional to M_T during acquisition. Thus, in a simple gradient echo sequence with a long TR, signal is proportional to the sine of the flip angle α, or proportional to $\sin(\gamma \int B_1^+ dt)$. While a slight variation of B_1^+ in a case with a flip angle near 90° may not be as noticeable, at low flip angles, signal intensity will be directly proportional to B_1^+. Effects of flip angle on image contrast can be understood by remembering that T_1 contrast depends on the amount of M_z that is available for an excitation pulse after a time

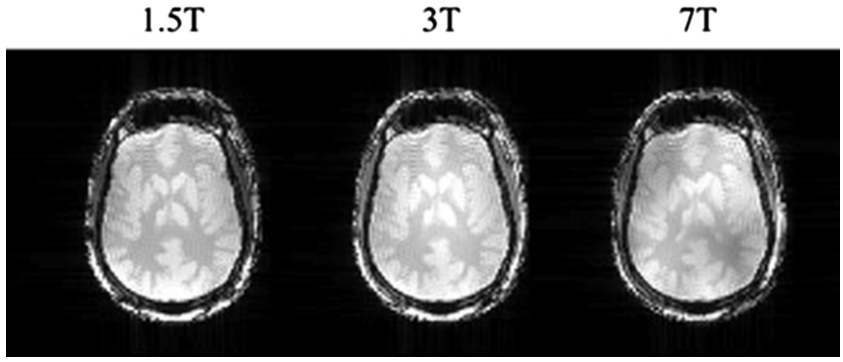

Figure 4.8. Signal intensity distribution affected by imperfect representation of the B_1^- field distributions during image reconstruction, in this case are more prominent at a higher field strength, where field distributions are affected more severely by the tissues of the individual subject.

TR has elapsed since the excitation pulse of a prior repetition. Thus, in a region with a smaller flip angle, M_z will be larger than expected, making it appear as if the tissues have a shorter T_1 than they actually do. A large number of methods to reduce B_1^+ inhomogeneity or its effects on the image have been developed through the years. At low frequencies, care in coil design and construction can be very beneficial, but at higher frequencies, where B_1 wavelengths and skin depths in tissue are not much larger than the imaging region, the field distributions vary from subject to subject and design of a single volume coil has limited benefit. Specialized pulses such as composite pulses [20] and adiabatic pulses [21] can produce very homogeneous flip angles even for inhomogeneous B_1^+ distributions, but at a cost of longer pulse durations and greater SAR and resultant tissue heating.

In reconstruction strategies where knowledge of the B_1^- field distributions of the receive coil(s) are used to create an image with uniform intensity [22], imperfect knowledge of the receive field distributions can result in image artifacts. While the clear solution to this is improving knowledge of receive coil field distributions, mapping of this in each subject can be tedious, as it can require first mapping the B_0 and B_1^+ fields to separate their effects on signal intensity from that of B_1^-. Figure 4.8 shows a simulated example of an image affected by imperfect representation of the B_1^- field distributions during image reconstruction [23].

It is important to note that MRI is extremely powerful and versatile, such that many of the physical phenomena that affect MR images can be measured with MRI using strategic sequences and image reconstruction strategies. For example, while motion and flow can cause image artifacts for some sequences, with specialized sequences and data processing it is possible to image and even quantitatively map motion [24] and flow [25]. Sequences have also been created to image diffusion and perfusion, and all these sequences are used routinely in patient care today. Similarly, MRI sequences have been developed to measure the B_0 field, the B_1 fields, tissue electrical and magnetic properties, and even temperature increase due to heating with RF energy. The next chapter will introduce some of these specialized sequences related to fields, tissue electromagnetic properties, and SAR-induced temperature increase.

Also, while in this section we have discussed the image artifacts due to field/tissue interactions, important anatomical and physiological information can also be gained from such field distortions. The most obvious examples are related to effects of tissue magnetic susceptibility on the B_0 field, especially with respect to the differences in magnetic susceptibility for oxygenated and deoxygenated blood. These differences are exploited to produce excellent visualization of blood vessels with susceptibility weighted imaging [26], and are at least partly responsible for the real-time changes in signal strength utilized in functional MRI [27] now used to explore differences in brain function between groups with various neurological disorders and to plan surgeries to avoid damaging regions associated with critical functions in individual patients.

References

[1] Yang B, Collins C M and Smith M B 2001 Calculation of static magnetic field distortions in a multi-tissue human head model for MRI *9th Scientific Meeting of the ISMRM* (Glasgow, UK) vol 616

[2] Bube R H 1992 *Electrons in Solids: An Introductory Survey* (New York: Academic)

[3] Foster K R and Schwan H P 1995 Dielectric properties of tissues *Handbook of Biological Effects of Electromagnetic Fields* **vol 2** 25–102

[4] Gabriel S, Lau R W and Gabriel C 1996 The dielectric properties of biological tissues: II. Measurements in the frequency range 10 Hz to 20 GHz *Phys. Med. Biol.* **41** 2251

[5] http://www.magresource.com/

[6] Kanal E *et al* 2007 ACR guidance document for safe MR practices: 2007 *Am. J. Roentgenol.* **188** 1447–74

[7] IEC 2010 *International Standard, Medical Equipment—Part 2: Particular Requirements for the Safety of Magnetic Resonance Equipment for Medical Diagnosis* 3rd edn (Geneva: International Electrotechnical Commission) 601-2-33.

[8] FDA 2003 *Guidance for Industry and FDA Staff—Criteria for Significant Risk Investigations of Magnetic Resonance Diagnostic Devices* http://www.fda.gov/cdrh/ode/guidance/793.pdf

[9] Chronik B A and Rutt B K 2001 Simple linear formulation for magnetostimulation specific to MRI gradient coil *Magn. Reson. Med.* **45** 916–9

[10] Collins C M and Smith M B 2001 Signal-to-noise ratio and absorbed power as functions of main magnetic field strength, and definition of '90°' RF pulse for the head in the birdcage coil *Magn. Reson. Med.* **45** 684–91

[11] Liu W, Collins C M and Smith M B 2005 Calculations of B_1 distribution, specific energy absorption rate, and intrinsic signal-to-noise ratio for a body-size birdcage coil loaded with different human subjects at 64 and 128 MHz *Appl. Magn. Reson.* **29** 5–18

[12] de Greef M, Ipek O, Raaijmakers A J, Crezee J and van den Berg C A 2013 Specific absorption rate intersubject variability in 7 T parallel transmit MRI of the head *Magn. Reson. Med.* **69** 1476–85

[13] Eichfelder G and Gebhardt M 2011 Local specific absorption rate control for parallel transmission by virtual observation points *Magn. Reson. Med.* **66** 1468–76

[14] Cao Z, Oh S, Otazo R, Sica C T, Griswold M A and Collins C M 2015 Complex difference constrained compressed sensing reconstruction for accelerated PRF thermometry with application to MRI-induced RF heating *Magn. Reson. Med.* **73** 1420–31

[15] Carluccio G, Bruno M and Collins C M 2015 Predicting long-term temperature increase for time-dependent SAR levels with a single short-term temperature response *Magn. Reson. Med.* At press doi:10.1002/mrm.25805

[16] Murbach M, Neufeld E, Pruessmann K P and Kuster N 2012 Safe MR scan times based on CEM43 tissue damage thresholds, using electromagnetic and thermal simulations with anatomically correct human models and considering local thermoregulation *Proc. 20th Scientific Meeting of ISMRM* (May 2012, Melbourne, Australia)

[17] Pusey E, Lufkin R B, Brown R K, Solomon M A, Stark D D, Tarr R W and Hanafee W N 1986 Magnetic resonance imaging artifacts: mechanism and clinical significance *Radiographics* **6** 891–911

[18] Anderson L J *et al* 2001 Cardiovascular *T*2-star (*T*2*) magnetic resonance for the early diagnosis of myocardial iron overload *Eur. Heart J.* **22** 2171–9

[19] Selim M, Fink J, Linfante I, Kumar S, Schlaug G and Caplan L R 2002 Diagnosis of cerebral venous thrombosis with echo-planar T2*-weighted magnetic resonance imaging *Arch. Neurol.* **59** 1021–6

[20] Levitt M H 1986 Composite pulses *Prog. Nucl. Magn. Reson. Spectrosc.* **18** 61–122

[21] Garwood M and DelaBarre L 2001 The return of the frequency sweep: designing adiabatic pulses for contemporary NMR *J. Magn. Reson.* **153** 155–77

[22] Roemer P B, Edelstein W A, Hayes C E, Souza S P and Mueller O M 1990 The NMR phased array *Magn. Reson. Med.* **16** 192–225

[23] Cao Z, Park J, Cho Z H and Collins C M 2015 Numerical evaluation of image homogeneity, signal-to-noise ratio, and specific absorption rate for human brain imaging at 1.5, 3, 7, 10.5, and 14 T in an 8-channel transmit/receive array *J. Magn. Reson. Imaging* **41** 1432–9

[24] Kim D, Dyvorne H A, Otazo R, Feng L, Sodickson D K and Lee V S 2012 Accelerated phase-contrast cine MRI using *k–t* SPARSE-SENSE *Magn. Reson. Med.* **67** 1054–64

[25] Mohiaddin R H, Gatehouse P D, Henien M and Firmin D N 1997 Cine MR Fourier velocimetry of blood flow through cardiac valves: comparison with Doppler echocardiography *J. Magn. Reson. Imaging* **7** 657–63

[26] Haacke E M, Xu Y, Cheng Y C N and Reichenbach J R 2004 Susceptibility weighted imaging (SWI) *Magn. Reson. Med.* **52** 612–8

[27] Ogawa S, Tank D W, Menon R, Ellermann J M, Kim S G, Merkle H and Ugurbil K 1992 Intrinsic signal changes accompanying sensory stimulation: functional brain mapping with magnetic resonance imaging *Proc. Natl Acad. Sci.* **89** 5951–5

IOP Concise Physics

Electromagnetics in Magnetic Resonance Imaging: Physical Principles, Related Applications, and Ongoing Developments

Christopher M Collins

Chapter 5

MRI-based measurement of field distributions and tissue heating

MRI is sensitive to a wide range of physical properties and physiological phenomena. With creative application of various pulses and timing of acquisitions, combined at times with use of exogenous contrast agents, it has become, for many purposes, the most valuable and versatile of medical imaging tools, capable of mapping fundamental tissue properties, brain function [1], diffusion [2], and perfusion [3], and even specific chemical species throughout the body [4]. While entire books could be (and are!) written on each one of these topics and many others, in this chapter we will focus on some of the potential and capabilities of particular interest in electromagnetics.

5.1 Mapping the static magnetic field distribution

Recognizing that the precessional frequency is proportional to the strength of the B_0 field and that the phase of the signal received is thus proportional to TE in any given repetition, it is possible to map the B_0 field from the difference in phase between two acquisitions with a variety of methods. The most easily understood is that of mapping the difference in signal phase between images acquired with slightly different values of TE. Taking the difference between these two phase images largely removes all other common sources of spatially dependent signal phase, such as those from the transmit and receive RF coils, and leaves only the effect of local B_0 field on the rate of nuclear precession. The difference in phase between the two images is thus proportional to the local B_0 times γ multiplied by the difference in TE between the two images [5].

doi:10.1088/978-1-6817-4083-6ch5

5.2 Mapping RF magnetic fields

Noting the proportionality between signal intensity in a gradient echo sequence and the sine of the flip angle, B_1^+ can be mapped by strategic acquisition of images having different flip angles. In one of the most straightforward methods, the double angle method, the ratio of signal strength of two gradient echo images acquired with identical parameters except one having twice the flip angle (i.e. twice the B_1^+ field strength) of the other is taken. Then the basic trigonometric relation [6]

$$\alpha_1 = \arccos\left(\frac{S_2}{2S_1}\right)$$

is utilized where α_1 is the location-dependent flip angle used to acquire the first image, which has location-dependent signal strength S_1, and the second image, having location-dependent signal strength S_2, was acquired with twice the flip angle of the first. A related method would be to acquire a series of images with increasing flip angles and then fit signal intensity at each location with a sinusoidal function. The main problem with these simple approaches is that to avoid effects of T_1 relaxation affecting the measurement, TR values must be very long—approximately five times the longest T_1 present in the imaging region [6]. Today a wide variety of more sophisticated methods to separate the effects of B_1^+ and T_1 on signal strength, and even map them both simultaneously very rapidly are available [7–9].

If the B_1^+ field is known (or can be assumed uniform, as is often done for a transmit birdcage coil at low frequencies), B_1^- can be discerned from the received signal using a variety of relatively simple methods. At low frequencies and homogeneous B_0, B_1^- for each coil is directly proportional to signal in the image acquired by that coil in a homogeneous phantom, and at low frequencies it may not be affected much by the imaging subject itself, so a single map of B_1^- fields in a homogeneous phantom may be reasonably accurate for imaging all subjects. Under these circumstances, an adequate map for each receive coil can often be produced by dividing the image acquired with the receive coil by an image acquired with the body birdcage coil, or by the sum-of-squares image (section 2.5) from all receive coils. These methods can also be applied with some success to individual patients to remove weighting of different tissues on the B_1^- maps. At high frequencies with transmit and receive arrays, and where the effects of B_0 inhomogeneity are more prominent, determination of B_1^+ and B_1^- maps can require use of B_1^+ mapping methods for all transmit coils individually while receiving from all coils simultaneously, as well as mapping of the B_0 field followed by an iterative or matrix-based approach to solve for all desired fields of all coils [10].

Determining the phase of B_1^+ and B_1^- fields also relies on a variety of methods, depending on the circumstances. First, phase is relative by nature, so it is possible to define any of a variety of references in the phase of the image. If it is possible to assume a homogeneous phase of the transmit coil (as, again, is often done for birdcage coils at low frequencies), and if B_0 can be considered homogeneous, then the phase of the received signal is proportional to the B_1^- field in each coil. For phase

of a single coil used in transmission and reception, assuming a homogeneous B_0 field, it can be assumed that one half of the phase evolution seen in the signal is due to transmission and the other half is due to reception, as it should take the same time for excitation fields to reach a given location as for the signal to reach the coil from that location.

5.3 Mapping RF-induced heating

Temperature affects a number of phenomena that the MR signal is sensitive to. Changes in temperature can be measured with MRI due to the temperature dependence of diffusion rates, T_1, T_2, or a shift in the proton resonance frequency (PRF) itself [11]. The dependence of PRF shift on temperature is the phenomenon most often exploited for mapping temperature change because it can be done rapidly and with high SNR and resolution compared to other methods.

The temperature dependence of the PRF can be characterized with a PRF shift coefficient α such that the local temperature difference ΔT between otherwise identical gradient echo images can be calculated as

$$\Delta T = \frac{\Delta\varphi}{\alpha\gamma B_0 TE}$$

where $\Delta\varphi$ is the local difference in phase in the two images. For pure water, α is approximately −0.01 parts per million per degree Celsius. In practice, $\Delta\varphi$ is typically corrected to adjust for background system-related phase drift, which can be calculated from the phase signal in biological fat or additional oil samples placed around the subject, as oil and fat have almost no PRF shift.

A typical procedure for using the PRF shift method is to acquire a baseline image (which can consist of a few averages to improve SNR) followed by a series of additional images during or interspersed with heating, then applying the above equation to calculate the temperature change between images. The source of heat can be pretty much anything, and is often high-intensity focused ultrasound [12], but electromagnetic sources including MR imaging coils [13], RF hyperthermia antenna arrays [14], RF or laser ablation probes [15, 16], or even cellular phones [17] have been used as well.

References

[1] Ogawa S, Tank D W, Menon R, Ellermann J M, Kim S G, Merkle H and Ugurbil K 1992 Intrinsic signal changes accompanying sensory stimulation: functional brain mapping with magnetic resonance imaging *Proc. Natl Acad. Sci.* **89** 5951–5

[2] Le Bihan D, Mangin J F, Poupon C, Clark C A, Pappata S, Molko N and Chabriat H 2001 Diffusion tensor imaging: concepts and applications *J. Magn. Reson. Imaging* **13** 534–46

[3] Buxton R B, Frank L R, Wong E C, Siewert B, Warach S and Edelman R R 1998 A general kinetic model for quantitative perfusion imaging with arterial spin labeling *Magn. Reson. Med.* **40** 383–96

[4] Maudsley A A, Domenig C, Govind V, Darkazanli A, Studholme C, Arheart K and Bloomer C 2009 Mapping of brain metabolite distributions by volumetric proton MR spectroscopic imaging (MRSI) *Magn. Reson. Med.* **61** 548–59

[5] Li S, Dardzinski B J, Collins C M, Yang Q X and Smith M B 1996 Three-dimensional mapping of the static magnetic field inside the human head *Magn. Reson. Med.* **36** 705–14
[6] Stollberger R and Wach P 1996 Imaging of the active B_1 field *in vivo Magn. Reson. Med.* **35** 246–51
[7] Sacolick L I, Wiesinger F, Hancu I and Vogel M W 2010 B_1 mapping by Bloch–Siegert shift *Magn. Reson. Med.* **63** 1315–22
[8] Treier R, Steingoetter A, Fried M, Schwizer W and Boesiger P 2007 Optimized and combined T_1 and B_1 mapping technique for fast and accurate T_1 quantification in contrast-enhanced abdominal MRI *Magn. Reson. Med.* **57** 568–76
[9] Voigt T, Nehrke K, Doessel O and Katscher U 2010 T_1 corrected B_1 mapping using multi-TR gradient echo sequences *Magn. Reson. Med.* **64** 725–33
[10] de Moortele V *et al* 2005 B_1 destructive interferences and spatial phase patterns at 7 T with a head transceiver array coil *Magn. Reson. Med.* **54** 1503–18
[11] Rieke V and Butts Pauly K 2008 MR thermometry *J. Magn. Reson. Imaging* **27** 376–90
[12] Ram Z *et al* 2006 Magnetic resonance imaging-guided, high-intensity focused ultrasound for brain tumor therapy *Neurosurgery* **59** 949–56
[13] Oh S, Ryu Y C, Carluccio G, Sica C T and Collins C M 2014 Measurement of SAR-induced temperature increase in a phantom and *in vivo* with comparison to numerical simulation *Magn. Reson. Med.* **71** 1923–31
[14] Gellermann J *et al* 2005 Methods and potentials of magnetic resonance imaging for monitoring radiofrequency hyperthermia in a hybrid system *Int. J. Hyperthermia* **21** 497–513
[15] Lewin J S *et al* 1998 Interactive MRI-guided radiofrequency interstitial thermal ablation of abdominal tumors: clinical trial for evaluation of safety and feasibility *J. Magn. Reson. Imaging* **8** 40–7
[16] Raz O *et al* 2010 Real-time magnetic resonance imaging–guided focal laser therapy in patients with low-risk prostate cancer *Eur. Urol.* **58** 173–7
[17] Alon L, Cho G Y, Yang X, Sodickson D K and Deniz C M 2015 A method for safety testing of radiofrequency/microwave-emitting devices using MRI *Magn. Reson. Med.* **74** 1397–405

IOP Concise Physics

Electromagnetics in Magnetic Resonance Imaging: Physical Principles, Related Applications, and Ongoing Developments

Christopher M Collins

Chapter 6

Recent and ongoing developments

The versatility of MRI presents seemingly endless possibilities for the future. New developments arise which, sometimes in just a few years, affect how MRI is performed in research and clinical practice. From an engineering perspective, the goals are often to increase speed and SNR, while other developments promise new information about the human body in the way of newly measureable physical or physiological properties. Here we briefly review a few of these most relevant to electromagnetics. As these methods currently have many different implementations, they will be described conceptually here with reference to more complete descriptions of specific approaches.

6.1 Parallel imaging

Besides facilitating an increase in SNR, receive coil arrays can be used to accelerate image acquisition. Because the signal received by each coil is weighted by a different spatial distribution according to the B_1^- field distribution of each coil in the array, the signal provides spatial information in addition to what is available through traditional spatial encoding with gradient fields. While some methods to accomplish this were proposed much earlier, in recent decades use of such parallel imaging techniques have become robust enough to be incorporated into routine clinical practice.

There are a number of approaches to accomplishing parallel imaging. Loosely they can be categorized into methods that operate in *k*-space [1, 2] or in the image domain [3]. Alternatively, they can be classified into methods that require *a priori* information about the coils' B_1^- field distributions [1, 3] and those that do not [2]. In modern implementations, these distinctions are less relevant, but here they are used to introduce basic concepts.

As an example of a well-known method operating in the image domain and utilizing *a priori* information, with SENSE [3] images from each coil can be created

doi:10.1088/978-1-6817-4083-6ch6

with a reduced number of lines in *k*-space, for example, by skipping every other line for a reduction factor of 2. While the image produced from the *k*-space data of each coil will then be aliased, or have information from multiple locations in the sample at each location in the image (giving a 'folded' appearance in the image), with *a priori* information about the coils' B_1^- field distributions and the information in these aliased images it is possible to construct a matrix equation to solve for signal from each location in the imaging subject [3].

As an example of a well-known method operating in *k*-space and not relying on *a priori* information, with GRAPPA [2] a reduced number of lines in *k*-space are acquired, for example, by skipping every other line for a reduction factor of 2. Then a few of the intermediate lines near the center of *k*-space are acquired, and weighting functions are determined that best fit the few intermediate lines from the acquired lines in all coils. These weighting functions are then used to fill the missing lines throughout *k*-space with the acquired lines from all coils [2].

In general, acceleration of the imaging process with parallel imaging methods results in a reduction of SNR as there are fewer total acquisitions, and the distribution of noise in parallel imaging methods is, in general, not uniform throughout the image [3]. There are also some artifacts particular to parallel imaging. For these reasons, parallel imaging methods must be used with caution and with awareness of their limitations.

6.2 Transmit coil arrays

The push towards higher B_0 field strengths for better SNR in MRI naturally requires higher B_1 frequencies. This results in shorter wavelengths and less homogeneous excitation fields, as well as higher SAR (via Faraday's law, for example) than at lower frequencies. Use of multiple coils, with different B_1^+ distributions, that can be driven independently has led to greater control of the B_1^+ fields and SAR through space and time. This comes at a cost of greater technical requirements in coil design, RF amplifiers, pulse design, and SAR assessment. Schemes for use of transmit arrays can be separated broadly into 'RF shimming' [4], where typically the B_1^+ field distribution is optimized for imaging the desired region in the coil, and 'parallel transmission' techniques [5, 6], in which the amplitude and phase of individual coils are varied through time, often in coordination with the gradient coils, during individual pulses to accomplish particular excitations of M through space. The advantages of transmit coil arrays have already begun to be adopted in clinical practice [7], with the two orthogonal ports of the system whole-body birdcage coil being driven independently, rather than with identical amplitudes and a set 90° degree phase difference. Also, related to the use of transmit coils and arrays at field strengths of 7 T and above is a growing interest in the use of array elements that are designed to be more radiative (rather than inductive) in nature, such as patch antennas and dipole antennas [8, 9]. In order to assess SAR for transmit arrays, it is necessary to consider the interactions between the coils as well as the power transmitted to and reflected from each coil [10]. Figure 6.1 shows simulated examples of variations in signal intensity and contrast across a single image due to inhomogeneous B_1^+ of the excitation coil and its

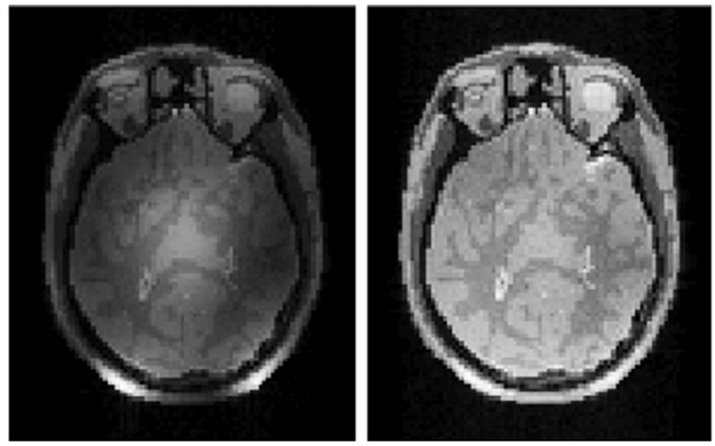

Figure 6.1. Variations in signal intensity and contrast across a single image due to inhomogeneous B_1^+ of the excitation coil (left) and its alleviation with use of a transmit array driven to produce a more homogeneous B_1^+ field distribution (right).

alleviation with use of a transmit array driven to produce a more homogeneous B_1^+ field distribution specific to the subject.

6.3 Gradient field monitoring

The gradient fields in MRI are comparatively stable, predictable, and insensitive to potential distortions due to physical interaction with the imaging subject for many basic sequences. At research sites where sequences with extremely rapid switching of gradient fields, very complex 3D trajectories through *k*-space, and/or pulse sequences extremely sensitive to patient motion are being implemented, monitoring of the actual gradient field strengths through time can be useful in the creation of accurate images [11–13]. Eddy currents induced in metallic components by rapidly switching gradients, slight nonlinearities in gradient amplifier performance and gradient field distributions, and field disturbances due to patient respiration and motion can all have subtle effects on the actual position in *k*-space, making it slightly different than that expected. By monitoring gradient field distributions through time, these deviations from the desired trajectory can be accounted for and corrected in reconstruction and/or in pulse programming. Gradient field monitoring today most often relies on use of a number of small RF probes, each having its own RF coil and its own liquid sample, and all probes having known positions through space in the magnet. The frequency of signals from these probes through time can then be used to track actual gradients through the imaging region.

6.4 High-permittivity materials and meta-materials for manipulating RF fields in MRI

Given the sensitivity of MRI to the strength of the RF magnetic field both in nuclear excitation and signal detection, a number of groups have experimented with use of

specialized passive materials to improve the performance of MRI in a variety of circumstances. Materials with high electric permittivity have been used to improve the signal locally within existing RF coils or arrays [14–17], or to create dielectric resonators which replace the conductive RF coils altogether [18, 19]. In a few instances, metamaterials constructed of strategic layering of conductive and non-conductive materials, strategic positioning of small resonators throughout space, or other methods [20, 21] have shown intriguing results. One major challenge to the routine use of any of these materials is the significant space they can require in the MRI system. Also, they are sometimes seen as a competitor to the increasingly available and very versatile transmit array (section 6.2). While early high-permittivity materials consisted primarily of water-based materials [14–16, 18], materials of increasingly high electric permittivity produced by either mixing high-permittivity ceramics in powder form [17] or ceramic beads [22] with water or use of solid ceramics [19] allow for reduction in the amount of material and space required to create a desired effect, and some recent studies show advantages to SNR and transmit homogeneity in excess of those provided by transmit and receive arrays alone [23, 24].

6.5 MR fingerprinting

One recently developed method of imaging relies heavily on *a priori* modeling of the MR signal through time as a function of both MR parameters (T_1, T_2, and proton density) and the fields they experience. In the first implementation [25], a library of pre-calculated timecourses of signal from a single location is generated for a wide range of possible T_1, T_2, and resonant frequencies (related to B_0 strength and chemical species present) with simulations of the Bloch equation for a pseudorandom sequence of pulses. This same sequence of pulses is then applied to the MRI system, and the best match in signal timecourse from each location is matched to its best fit in the library, thus quantitatively determining the T_1, T_2, and B_0 (or chemical shift) as well as signal intensity (proportional to M_0 and receive coil sensitivity) at that location. In one recent variation [26], the pre-computed library also includes B_1^+ from different coils in a transmit array such that B_1^+ from each coil is also mapped in the process. While at this time it is uncertain how this new method will affect the future of MRI, it is an excellent example of a creative approach producing promising new developments which, at the same time, can map B_0 and B_1^+ field distributions.

6.6 Measurement of tissue electromagnetic properties

In MRI, the B_0 and B_1 fields are functions of both the magnets (or coils) that produce them and their interactions with the tissues in the human body. In recent years there have been increasing efforts to utilize information in the spatial distribution of B_0 and B_1 fields to determine the electromagnetic properties, specifically the DC magnetic susceptibility from B_0, and the RF permittivity and conductivity from B_1.

With quantitative susceptibility mapping, a series of manipulations of a B_0 map are performed to remove gradual variations due to overall B_0 inhomogeneity resulting from imperfections in shimming and air/tissue interfaces to (ideally) leave

only those variations in B_0 due to tissue magnetic susceptibility. Then a regional inversion of a specific form of Gauss's law for magnetism is performed to solve for tissue susceptibility [27].

In MR electrical properties tomography, knowledge of the B_1^+ distribution from one or more coils as mapped with MR methods is used as an input to the Helmholtz equation (or other combination of the Maxwell equations not relying on direct knowledge of electric fields) to solve for the local electrical properties σ and ε_r [28]. While different implementations have shown various levels of success in different situations, some shortcomings of the method include a lack of knowledge of any z-oriented component of the B_1 field (which is often assumed to be zero near the center of a birdcage coil, loop coil, or dipole antenna), the need to calculate second derivatives of the B_1^+ field distribution through space (making results very sensitive to noise), and the assumption of piecewise-constant electrical properties necessary to apply the kernels solving for them. Work is ongoing, and different recent approaches are designed to reduce or eliminate some or all of these issues [28, 29].

References

[1] Sodickson D K and Manning W J 1997 Simultaneous acquisition of spatial harmonics (SMASH): fast imaging with radiofrequency coil arrays *Magn. Reson. Med.* **38** 591–603

[2] Griswold M A *et al* 2002 Generalized autocalibrating partially parallel acquisitions (GRAPPA) *Magn. Reson. Med.* **47** 1202–10

[3] Pruessmann K P, Weiger M, Scheidegger M B and Boesiger P 1999 SENSE: sensitivity encoding for fast MRI *Magn. Reson. Med.* **42** 952–62

[4] Metzger G J, Snyder C, Akgun C, Vaughan T, Ugurbil K and de Moortele V 2008 Local B_1^+ shimming for prostate imaging with transceiver arrays at 7 T based on subject-dependent transmit phase measurements *Magn. Reson. Med.* **59** 396–409

[5] Zhu Y 2004 Parallel excitation with an array of transmit coils *Magn. Reson. Med.* **51** 775–84

[6] Katscher U, Börnert P, Leussler C and Van Den Brink J S 2003 Transmit sense *Magn. Reson. Med.* **49** 144–50

[7] Childs A S, Malik S J, O'Regan D P and Hajnal J V 2013 Impact of number of channels on RF shimming at 3 T *Magn. Reson. Mater. Phys. Biol. Med.* **26** 401–10

[8] Brunner D O, De Zanche N, Fröhlich J, Paska J and Pruessmann K P 2009 Travelling-wave nuclear magnetic resonance *Nature* **457** 994–8

[9] Raaijmakers A J E, Ipek O, Klomp D W J, Possanzini C, Harvey P R, Lagendijk J J W and Van den Berg C A T 2011 Design of a radiative surface coil array element at 7 T: the single-side adapted dipole antenna *Magn. Reson. Med.* **66** 1488–97

[10] Zhu Y, Alon L, Deniz C M, Brown R and Sodickson D K 2012 System and SAR characterization in parallel RF transmission *Magn. Reson. Med.* **67** 1367–78

[11] Barmet C, De Zanche N and Pruessmann K P 2008 Spatiotemporal magnetic field monitoring for MR *Magn. Reson. Med.* **60** 187–97

[12] Wilm B J, Barmet C, Pavan M and Pruessmann K P 2011 Higher order reconstruction for MRI in the presence of spatiotemporal field perturbations *Magn. Reson. Med.* **65** 1690–701

[13] Vannesjo S J, Haeberlin M, Kasper L, Pavan M, Wilm B J, Barmet C and Pruessmann K P 2013 Gradient system characterization by impulse response measurements with a dynamic field camera *Magn. Reson. Med.* **69** 583–93

[14] Alsop D C, Connick T J and Mizsei G 1998 A spiral volume coil for improved RF field homogeneity at high static magnetic field strength *Magn. Reson. Med.* **40** 49–54
[15] Yang Q X *et al* 2006 Manipulation of image intensity distribution at 7.0 T: passive RF shimming and focusing with dielectric materials *J. Magn. Reson. Imaging* **24** 197–202
[16] Yang Q X, Wang J, Wang J, Collins C M, Wang C and Smith M B 2011 Reducing SAR and enhancing cerebral signal-to-noise ratio with high permittivity padding at 3 T *Magn. Reson. Med.* **65** 358–62
[17] Teeuwisse W M, Brink W M and Webb A G 2012 Quantitative assessment of the effects of high-permittivity pads in 7 tesla MRI of the brain *Magn. Reson. Med.* **67** 1285–93
[18] Wen H, Jaffer F A, Denison T J, Duewell S, Chesnick A S and Balaban R S 1996 The evaluation of dielectric resonators containing H_2O or D_2O as RF coils for high-field MR imaging and spectroscopy *J. Magn. Reson. B* **110** 117–23
[19] Neuberger T, Tyagi V, Semouchkina E, Lanagan M, Baker A, Haines K and Webb A G 2008 Design of a ceramic dielectric resonator for NMR microimaging at 14.1 tesla *Concepts Magn. Reson B* **33** 109–14
[20] Algarin J M, Lopez M A, Freire M J and Marques R 2011 Signal-to-noise ratio evaluation in resonant ring metamaterial lenses for MRI applications *New J. Phys.* **13** 115006
[21] Freire M J, Marques R and Jelinek L 2008 Experimental demonstration of a $\mu = -1$ metamaterial lens for magnetic resonance imaging *Appl. Phys. Lett.* **93** 231108
[22] Luo W *et al* 2013 Permittivity and performance of dielectric pads with sintered ceramic beads in MRI: early experiments and simulations at 3 T *Magn. Reson. Med.* **70** 269–75
[23] Brink W M and Webb A G 2014 High permittivity pads reduce specific absorption rate, improve B_1 homogeneity, and increase contrast-to-noise ratio for functional cardiac MRI at 3 T *Magn. Reson. Med.* **71** 1632–40
[24] Collins C M, Carluccio G, Vaidya M V, Haemer G G, Luo W, Lattanzi R, Wiggins G, Sodickson D K and Yang Q X 2014 High-permittivity materials can improve global performance and safety of close-fitting arrays *Proc. ISMRM 23rd Annual Meeting (May 10–16, 2014, Milan)* p 404
[25] Ma D, Gulani V, Seiberlich N, Liu K, Sunshine J L, Duerk J L and Griswold M A 2013 Magnetic resonance fingerprinting *Nature* **495** 187–92
[26] Cloos M, Wiggins C, Wiggins G and Sodickson D 2014 Plug and play parallel transmission at 7 and 9.4 tesla based on principles from MR fingerprinting *Joint Annual Meeting ISMRM-ESMRMB*
[27] de Rochefort L *et al* 2010 Quantitative susceptibility map reconstruction from MR phase data using Bayesian regularization: validation and application to brain imaging *Magn. Reson. Med.* **63** 194–206
[28] Voigt T, Katscher U and Doessel O 2011 Quantitative conductivity and permittivity imaging of the human brain using electric properties tomography *Magn. Reson. Med.* **66** 456–66
[29] Marques J P, Sodickson D K, Ipek O, Collins C M and Gruetter R 2014 Single acquisition electrical property mapping based on relative coil sensitivities: a proof-of-concept demonstration *Magn. Reson. Med.* **74** 185–95

IOP Concise Physics

Electromagnetics in Magnetic Resonance Imaging: Physical Principles, Related Applications, and Ongoing Developments

Christopher M Collins

Chapter 7

Conclusion

MRI is a valuable and dynamic medical imaging technology relying on a range of magnetic field strengths, distributions, and frequencies like no other used routinely in the human body. It relies on techniques and technologies which present both very interesting challenges and very exciting opportunities.

In this work we have covered the fundamentals required to understand the relationship of the quality, speed, and safety of MRI to the distributions of electromagnetic fields and their interactions with human tissues throughout space. We have also summarized (with reference to more complete descriptions) a variety of existing and evolving methods to improve MRI with better understanding and/or more creative manipulation of the fields throughout the body.

While MRI is, on the one hand, a relatively well-developed medical imaging technique, as is demonstrated over and over again, understanding of its current implementations combined with creative application of new ideas can lead to improvement in the quality, speed, and nature of information acquired with MRI both now and in the future.

doi:10.1088/978-1-6817-4083-6ch7